Monthly Notices of the ROYAL ASTRONOMICAL SOCIETY

Mon. Not. R. Astron. Soc. **425,** 930–949 (2012) doi:10.1111/j.1365-2966.2012.21341.x

On the HU Aquarii planetary system hypothesis

Krzysztof Goździewski,[1⋆] Ilham Nasiroglu,[2,3] Aga Słowikowska,[4] Klaus Beuermann,[5] Gottfried Kanbach,[2] Bartosz Gauza,[6,7] Andrzej J. Maciejewski,[4] Robert Schwarz,[8] Axel D. Schwope,[8] Tobias C. Hinse,[9] Nader Haghighipour,[10] Vadim Burwitz,[2,11] Mariusz Słonina[1] and Arne Rau[2]

[1]*Toruń Centre for Astronomy, Nicolaus Copernicus University, Gagarin Str. 11, 87-100 Toruń, Poland*
[2]*Max Planck Institute for Extraterrestrial Physics, Giessenbachstrasse, 85748 Garching, Germany*
[3]*Department of Physics, University of Cukurova, 01330 Adana, Turkey*
[4]*Kepler Institute of Astronomy, University of Zielona Góra, Lubuska 2, 65-265 Zielona Góra, Poland*
[5]*Institut für Astrophysik, Universität Goettingen, Friedrich-Hund-Platz 1, DE 37077 Göttingen, Germany*
[6]*Instituto de Astrofísica de Canarias (IAC), E-38200 La Laguna, Tenerife, Spain*
[7]*Dept. Astrofísica, Universidad de La Laguna (ULL), E-38206 La Laguna, Tenerife, Spain*
[8]*Leibniz-Institute für Astrophysik (AIP), An der Sternwarte 16, 14482 Potsdam, Germany*
[9]*Korea Astronomy and Space Science Institute (KASI), Optical Astronomy Research Center, 776 Daedukdae-ro, Daejeon 305-348, Republic of Korea*
[10]*Institute for Astronomy and NASA Astrobiology Institute, University of Hawaii-Manoa, 2680 Woodlawn Drive, Honolulu, HI 96822, USA*
[11]*Observatorio Astronomico de Mallorca, 07144 Costitx, Mallorca, Spain*

Accepted 2012 May 15. Received 2012 May 4; in original form 2012 March 1

ABSTRACT

In this paper, we investigate the eclipse timing of the polar binary HU Aquarii that has been observed for almost two decades. Recently, Qian et al. attributed large (O–C) deviations between the eclipse ephemeris and observations to a compact system of two massive Jovian companions. We improve the Keplerian, kinematic model of the light travel time effect and re-analyse the whole currently available data set. We add almost 60 new, yet unpublished, mostly precision light curves obtained using the time high-resolution photopolarimeter Optical Timing Analyzer (OPTIMA), as well as photometric observations performed at the Monitoring Network of Telescopes/North, Physics Innovations Robotic Astronomical Telescope Explorer and Carlos Sánchez Telescope. We determine new mid-egress times with a mean uncertainty at the level of 1 s or better. We claim that because the observations that currently exist in the literature are non-homogeneous with respect to spectral windows (ultraviolet, X-ray, visual and polarimetric mode) and the reported mid-egress measurements errors, they may introduce systematics that affect orbital fits. Indeed, we find that the published data, when taken literally, cannot be explained by any unique solution. Many qualitatively different and best-fit two-planet configurations, including self-consistent, Newtonian *N*-body solutions may be able to explain the data. However, using high-resolution, precision OPTIMA light curves, we find that the (O–C) deviations are best explained by the presence of a single circumbinary companion orbiting at a distance of ∼4.5 au with a small eccentricity and having ∼7 Jupiter masses. This object could be the next circumbinary planet detected from the ground, similar to the announced companions around close binaries HW Vir, NN Ser, UZ For, DP Leo, FS Aur or SZ Her, and planets of this type around Kepler-16, Kepler-34 and Kepler-35.

Key words: methods: data analysis – methods: numerical – techniques: photometric – celestial mechanics – planets and satellites: dynamical evolution and stability.

1 INTRODUCTION

Magnetic cataclysmic variables (CVs, polars, also known as AM Her stars) are interacting close binary systems. They consist of a main-sequence red dwarf secondary filling its Roche lobe, and a strongly magnetized white dwarf (WD) primary, with typical magnetic field values of 10–80 MG (Schwope et al. 2001). The strong magnetic field of the primary interacts with the weaker magnetic field of the secondary and locks the two stars together. Hence, the synchronously rotating WD spins at the same rate as the orbital mean motion of the binary. Under the gravitational field of the

⋆E-mail: k.gozdziewski@astri.uni.torun.pl

primary, material flows from the donor star initially along the binary orbital plane, and finally is accreted quasi-radially onto the magnetic poles of the WD. The variable HU Aquarii system (hereafter HU Aqr) belongs to this class of CV binaries hosting a strongly magnetic WD accompanied by a red dwarf (spectral type M4V) with an orbital period of about 125 min. This system is one of the brightest polars in the optical domain with visual magnitudes ranging from 14.6 to 18 (Warner 1995; Hellier 2001), as well as in the X-ray energy range. Therefore, it has also been one of the most studied systems so far.

Accreted matter leaving from the red dwarf is initially not affected by the magnetic field of the WD. The matter follows a ballistic trajectory up to the moment when the WD magnetic field begins to dominate. Because the WD magnetosphere extends beyond the L_1 radius, the plasma stream cannot orbit freely, and thus does not form an accretion disc, unlike in other non-magnetic CVs. The accreted matter follows the magnetic field lines and forms an accretion spot at the magnetic poles of the WD. In many systems, the WD magnetic field is tilted in such a way that one magnetic pole is oriented towards the direction of flowing matter. Eclipses observed in highly inclined polars provide information about the stream geometry.

According to the most recent work of Schwope et al. (2011) the inclination of the binary is $\sim 87^\circ \pm 0\overset{\circ}{.}8$. This special geometry is important for the planetary hypothesis investigated in this work. Assuming that a planetary companion (or companions) has formed in the circumbinary disc, the inclination constraint removes the mass indeterminacy inherent to the eclipse timing method.

Recently, the HU Aqr system has received much attention in the literature. Schwarz et al. (2009) carried out an analysis of the light curves of the system and derived mid-egress times of the polar. They proposed a planetary companion as one possible explanation of the detected (O–C) variability. Shortly after this work, Qian et al. (2011) presented and discussed 10 new light curves in the optical domain. These authors confirmed the deviations of the observed mid-egress times from a linear or quadratic ephemeris, concluding that the large (O–C) residuals may be explained by the light travel time (LTT, also known as Roemer effect; Irwin 1952) due to two Jovian-mass planetary companions in orbits with semimajor axes of a few astronomical unit (au) and a moderate eccentricity of ~ 0.5 for the outer planet. The orbit of the inner planet was fixed to be circular. The ratio of the orbital periods of these massive putative planets would be presumably in a low-order 2c:1b mean motion resonance (MMR). The latter points to significant mutual interactions between these objects which strongly affects the orbital stability of the system. Indeed, shortly after that work was published, Horner et al. (2011) performed dynamical analysis of the putative HU Aqr two-planet system, exploring the parameter space within 3σ uncertainty levels of the derived Keplerian elements. They found that none of the best-fit configurations presented by Qian et al. (2011) was dynamically stable implying that the planetary hypothesis proposed by these authors is hard to maintain. After a few months, in a new paper, Wittenmyer et al. (2012) also re-analysed data in Qian et al. (2011) confirming that the two-planet configuration is mathematically consistent with the observations, but inferred orbits are catastrophically unstable over a $\sim 10^3$–10^4 yr time-scale. Furthermore, in a very recent paper, Hinse et al. (2012) improved the Keplerian fit models of this system by imposing orbital stability constraints on the objective function $(\chi^2_\nu)^{1/2}$. Although these authors were able to find a *stable* two-planet configuration consistent with the linear ephemeris model, orbital parameters of these planets were relatively distant from the formal best-fit solution by more than 3σ. Because the results of extensive dynamical analysis contradict the two-planet hypothesis, an alternative explanation of the (O–C) diagrams needs to be considered.

Long-term monitoring of HU Aqr shows large variations of the accretion rate that could be correlated with a migration of the accretion spot. Taking into account the observed changes of the accretion geometry during different accretion states, high and intermediate ones, Schwope et al. (2001) estimated the possible time-shift of eclipses to be on the level of 2 s, which is still much smaller than the deviations between the theoretical ephemeris and observed mid-egress moments. These results suggest that the migration of the accretion spot cannot be responsible for the (O–C) deviations, and we therefore rule it out.

The (O–C) variability of HU Aqr can be also attributed to other complex astrophysical phenomena in the binary, such as the Applegate mechanism and/or magnetic braking discussed by Schwarz et al. (2009) and Wittenmyer et al. (2012). The timing signal might also be affected by non-Gaussian red noise, which is a well known effect present in the precision photometry of transiting planets and timing of millisecond pulsars (e.g. Pont, Zucker & Queloz 2006; Coles et al. 2011). Hence, it should be stressed that we focus here on the planetary hypothesis, as one of the possible, simple and somehow attractive explanations of the (O–C) variability. We try to solve 'the puzzle' of unstable two-planet models through a new and independent analysis of available data, conducted along three basic directions.

The first one relies on the re-analysis of published data, because we found a few inconsistencies in the literature. Surprisingly, while in the recent paper, Wittenmyer et al. (2012) take into account 82 mid-egress points from Schwarz et al. (2009) and Qian et al. (2011), this is not the full data set available in the literature at that time. In fact, 72 egress times published by Schwarz et al. (2009) extend the data set in Schwope et al. (2001) that included 31 measurements. Although the early data of Schwope et al. (2001) spanning cycles 0–22 478 overlap with measurements in Schwarz et al. (2009) in the time window covering cycles 1319–60 097, they may be helpful to constrain the best-fit models. Up to now, the full list of published observations consists of 113 points, including data in Qian et al. (2011). Yet it is not quite obvious whether Qian et al. (2011) included measurements in Schwope et al. (2001) in their analysis. Hinse et al. (2012) considered the full data set available at that time, but in terms of the linear ephemeris LTT model only. In this context, a direct comparison of the results in the published papers is difficult.

The second aspect of our study is a new kinematic model of the ephemeris that properly approximates orbits of putative companions in multibody systems (to the lowest possible order in the masses), as compared to the full N-body model. The kinematic model used in all cited papers refers back to Keplerian parametrization by Irwin (1952) *for the 'one companion' case*. That model, though commonly used in the literature (e.g. Lee et al. 2012), seems nowadays redundant, as it was introduced to quantify a similarity between the LTT and the radial velocity curves, in a particular reference frame with the origin at the centre of the two-body LTT orbit (instead of the dynamical barycentre). Indeed, the recent, although short history of modelling precision radial velocities teaches us that multiple planetary systems should be modelled either using kinematic formulation in a proper coordinate frame (e.g. Goździewski, Konacki & Maciejewski 2003; Lee & Peale 2003), or using the most general and accurate full N-body model (Laughlin & Chambers 2001). The dynamical stability can be further incorporated as an additional, *implicit* observable to the objective function (e.g. Goździewski & Maciejewski 2001; Goździewski, Migaszewski & Musieliński 2008). In this work we focus on the kinematic modelling although the self-consistent N-body approach has also been used to analyse the HU Aqr mid-egress times (see Appendix A). Our results indicate that the Newtonian model may be required for other systems presumably exhibiting the LTT effect, indeed.

The third and, actually, critical direction of our work, is a careful independent analysis of the significantly extended data set including already published egress times, and new high-precision timing of the egresses obtained with the ultrafast photometer Optical Timing Analyzer (OPTIMA; Kanbach et al. 2003, 2008), as well as the Monitoring Network of Telescopes/North (MONET/N), Physics Innovations Robotic Astronomical Telescope Explorer (PIRATE) and Carlos Sánchez Telescope (TCS). We collected almost 60 new egress times with superior accuracy at the subsecond level. Moreover, we found that the literature data are non-homogeneous, as they come from different instruments with different time resolutions, as well as working in different spectral windows (from the visual range, through the UV, to the X-ray domain) and non/polarimetric modes. Taking into account the above-mentioned inhomogeneity factors and new data, we present the results from a quasi-global optimization of two basic LTT models, leading us to the conclusion that the measured (O–C) data of HU Aqr may be best explained by a one-planet configuration. Simultaneously, it would resolve the two-companion instability paradox in the simplest way.

This paper is structured as follows. In Section 2 we derive two-planet LTT models on the basis of Jacobi coordinates which describes kinematic orbits in multiple systems properly, as well as a hybrid optimization algorithm and numerical set-up that makes it possible to explore the $(\chi^2_\nu)^{1/2}$ parameter space in a quasi-global manner. We also briefly describe the N-body formulation of the LTT effect. In Section 3, we re-analyse the data set published in the literature, following the two-planet hypothesis by Qian et al. (2011) and further investigated by Wittenmyer et al. (2012). Two examples of highly degenerate best-fit solutions are found. In Section 4, possible effects of different spectral windows for the light curves and determination of egress times are studied. Furthermore, we describe the new data set derived with the OPTIMA and other instruments. In Section 5, we propose a one-planet model that best explains the (O–C) variability. We briefly discuss the effect of red noise in Section 6 and present a summary of our work in the Conclusions, Section 7. Appendix A contains extensive supplementary material to Section 5, including the results of kinematic and N-body modelling of two-planet systems, accompanied by the long-term stability tests.

2 LTT MODEL FOR A TWO-PLANET SYSTEM

We briefly develop the Keplerian model of the LTT signal in the three-body configuration, assuming that a compact binary (like HU Aqr) has *two* planetary companions. More technical details and a generalization of that model will be published elsewhere (Gozdziewski et al., in preparation). We consider the compact binary as a *single* object having the mass of m_*, which is reasonable in accordance with the extremely short orbital period (∼125 min) of the polar. A single companion, as well as multiple-planet models are particular cases of this problem. The key point is that the Keplerian (or *kinematic*) model requires special coordinates in order to preserve the sense of Keplerian elements as an approximation of the *exact* N-body initial condition. That can be accomplished by expressing the dynamics through particular canonical coordinates in which the mutual planetary interactions are possibly small with respect to the main, 'pure' Keplerian part. The barycentric formulation (Irwin 1952) in fact ignores the interactions which could be adequate for low-mass circumbinary objects, but it might fail when they have stellar masses as in the SZ Her system (Lee et al. 2012) where companions are as massive as 20 per cent of $M_\odot$, and can shift the system barycentre significantly. The reason for introducing this improved model is in fact the same as in the precision radial velocities analyses (e.g. Goździewski et al. 2003; Lee & Peale 2003).

2.1 Kinematic parametrization of the LTT effect

One of the well-known frames that provide a proper description of kinematic orbits in multiple systems is Jacobi coordinates. Let us assume that m_*, m_1 and m_2 represent the masses of the compact binary m_* and two planets, respectively. Let us also assume that the Cartesian coordinates of these objects with respect to the three-body barycentre are $\boldsymbol{R}_*$, $\boldsymbol{R}_1$, $\boldsymbol{R}_2$, and their Jacobi coordinates are denoted by $\boldsymbol{r}_* \equiv \boldsymbol{R}_*$, $\boldsymbol{r}_1$, $\boldsymbol{r}_2$ (see Fig. 1). Here $\boldsymbol{R}_*$ is the position of the centre of mass of the binary (CMB) in the barycentric frame, and $\boldsymbol{r}_1$, $\boldsymbol{r}_2$ are position vectors of the planetary companions in the Jacobi frame. In this formalism, the barycentric position of the binary is

$$\boldsymbol{R}_* = -\kappa_1 \boldsymbol{r}_1 - \kappa_2 \boldsymbol{r}_2, \tag{1}$$

where the mass factor coefficients $\kappa_1 \geq 0$, $\kappa_2 \geq 0$ are given by

$$\kappa_1 = \frac{m_1}{m_1 + m_*}, \quad \kappa_2 = \frac{m_2}{m_1 + m_2 + m_*}. \tag{2}$$

The coordinate transformation $\boldsymbol{R} \to \boldsymbol{r}$ is taken from Malhotra (1993):

$$\begin{aligned} \boldsymbol{r}_* &\equiv \boldsymbol{R}_*, \\ \boldsymbol{r}_1 &= \boldsymbol{R}_1 - \boldsymbol{R}_*, \\ \boldsymbol{r}_2 &= \boldsymbol{R}_2 - \frac{m_* \boldsymbol{R}_* + m_1 \boldsymbol{R}_1}{m_1 + m_*}, \end{aligned} \tag{3}$$

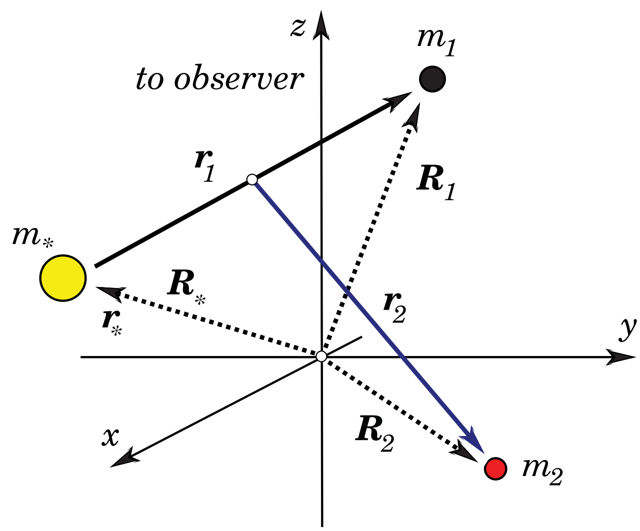

Figure 1. The geometry of the system. The binary has a total mass m_* and because of its short orbital period it can be considered as a point-like object accompanied by planets as point masses. The origin of the coordinate system is fixed at the barycentre of the three-body system. The line-of-sight is along the z-axis. See the text for more details.

and the inverse transformation is derived from the integral of the barycentre:

$$\begin{aligned}\boldsymbol{R}_* &= -\kappa_1 \boldsymbol{r}_1 - \kappa_2 \boldsymbol{r}_2,\\ \boldsymbol{R}_1 &= (1-\kappa_1)\boldsymbol{r}_1 - \kappa_2 \boldsymbol{r}_2,\\ \boldsymbol{R}_2 &= (1-\kappa_2)\boldsymbol{r}_2.\end{aligned} \tag{4}$$

To the first order in the mass ratio ($\sim m_{1,2}/m_*$), the true N-body orbit of body i ($i = 1, 2$) is described through geometric Keplerian elements as follows:

$$\boldsymbol{r}_i(t) = \boldsymbol{P}_i\,[\cos E_i(t) - e_i] + \boldsymbol{Q}_i \sqrt{1-e_i^2}\,\sin E_i(t),$$

where

$$\boldsymbol{P}_i = a_i\,(\boldsymbol{l}_i \cos\omega_i + \boldsymbol{k}_i \sin\omega_i)\,, \quad \boldsymbol{Q}_i = a_i\,(-\boldsymbol{l}_i \sin\omega_i + \boldsymbol{k}_i \cos\omega_i)\,,$$

and geometric elements are defined through

$$\boldsymbol{l}_i = \begin{bmatrix} +\sin\Omega_i \\ +\cos\Omega_i \\ 0 \end{bmatrix}, \qquad \boldsymbol{k}_i = \begin{bmatrix} +\cos i_i \cos\Omega_i \\ -\cos i_i \sin\Omega_i \\ \sin i_i \end{bmatrix}.$$

Here, $E_i(t)$ is the eccentric anomaly derived from the Kepler equation:

$$n_i(t - T_i) = E_i(t) - e_i \sin E_i(t),$$

where $n_i = 2\pi/P_i$ is the mean motion, in accordance with Kepler third law, $n_i^2 a_i^3 = \mu_i$, where P_i is the orbital period of a given object. Two tuples (a_i, e_i, i_i, Ω_i, ω_i, T_i), $i = 1, 2$, that consist of the semimajor axis, eccentricity, inclination, nodal angle, argument of pericentre and the time of pericentre passage, respectively, are for the geometric Keplerian elements. These are related to the Cartesian coordinates in the Jacobi frame through the usual two-body formulae (see e.g. Morbidelli 2002), with an appropriate mass parameter μ_i (see below).

From equation (1), the Z_* component of the CMB with respect to the system barycentre is

$$Z_*(t) \equiv \boldsymbol{R}_* \cdot \boldsymbol{e}_z = -\kappa_1 z_1(t) - \kappa_2 z_2(t), \tag{5}$$

where $\boldsymbol{e}_z$ is the unit vector along the z-axis of the reference frame, directed towards the observer. The signal contribution due to a given companion is

$$z_i(t) = a_i \sin i_i \left[\sin\omega_i\,(\cos E_i(t) - e_i) + \cos\omega_i \sqrt{1-e_i^2}\,\sin E_i(t)\right] \tag{6}$$

(for planets $i = 1, 2$). The $z_i(t)$ are then combined to obtain the $Z_*(t)$ component of the CMB position vector with respect to the system barycentre. The LTT signal is then expressed as

$$\tau(t) = -\frac{1}{c} Z_* \equiv +\frac{1}{c}\left(\frac{m_1}{m_1 + m_*} z_1 + \frac{m_2}{m_1 + m_2 + m_*} z_2\right),$$

where c is the speed of light. Note that we used the planetary version of the three-body system, with *one* dominant mass (m_*), hence the gravitational Keplerian parameters are

$$\mu_1 = k^2(m_1 + m_*), \quad \mu_2 = k^2 \frac{m_*(m_1 + m_2 + m_*)}{m_1 + m_*},$$

consistent with the expansion of the Hamiltonian perturbation for the planetary version of the problem (see e.g. Malhotra 1993), and the quantity k denotes the Gauss constant.

We introduce the signal semi-amplitude factors, K_1 and K_2 as

$$K_1 = \left(\frac{1}{c}\right) \frac{m_1}{m_1 + m_*} a_1 \sin i_1, \tag{7}$$

$$K_2 = \left(\frac{1}{c}\right) \frac{m_2}{m_1 + m_2 + m_*} a_2 \sin i_2. \tag{8}$$

Using equation (6), the single-planet signal contributions ζ_i are then given by

$$\zeta_i(t) = K_i \left[\sin\omega_i\,(\cos E_i(t) - e_i) + \cos\omega_i \sqrt{1-e_i^2}\,\sin E_i(t)\right]. \tag{9}$$

In this equation, the set of free orbital parameters is (K_i, P_i, e_i, ω_i, T_i), $i = 1, 2$, similar to the common kinematic radial velocity model. The orbital period P_i and the time of pericentre passage are introduced indirectly through the time dependence expressed by $E_i(t)$.

We would like to note here that the contribution of the planet as expressed in Irwin's model has an extra term $e_i \sin\omega_i$ that appears due to the particular choice of the coordinate system with the origin at the centre of the binary orbit around the common centre of mass of the system. It should also be stressed that no simple superposition of kinematic orbits does account for the mutual gravitational interactions directly, but in our formulation, the Keplerian elements are the closest to the osculating N-body initial condition within the kinematic model.

2.2 The (O − C) formulation

From equation (9), the fit model of the planetary-induced LTT signal is

$$\tau(t, K_1, P_1, e_1, \omega_1, T_1, K_2, P_2, e_2, \omega_2, T_2) = \zeta_1(t) + \zeta_2(t).$$

Now let us assume that the observational data are given through eclipse cycle number l ($l = 0, \ldots, N$), the date of the eclipse time-mark t_l, and its uncertainty σ_l. Then the l-cycle eclipse ephemeris with respect to the reference epoch t_0 ($l = 0$), at time $t \equiv t_l$ may be written as follows:

$$T_{\mathrm{ep}}(l) = t_0 + l P_{\mathrm{bin}} + \tau(t_l, K_{1,2}, P_{1,2}, e_{1,2}, \omega_{1,2}, T_{1,2}) + \text{‘physics’},$$

where P_{bin} is the orbital period of the binary. This period should not be assumed as known in advance, hence must be fitted, along with the initial epoch t_0 corresponding to cycle number $l = 0$, simultaneously with other parameters of the model. The term coded as ‘physics’ contains *non-Keplerian* effects, such as the period damping or other phenomena that may/should be included in the fit model. Here, we introduce two instances of such a model. Following Hilditch (2001), the *linear ephemeris* model, defined as above,

$$(\mathrm{O-C}) = T_{\mathrm{ep}}(l) - t_0 - l P_{\mathrm{bin}} = \tau(t_l, K_{1,2}, P_{1,2}, e_{1,2}, \omega_{1,2}, T_{1,2}), \tag{10}$$

and the *quadratic ephemeris* model, the simplest, yet non-trivial generalization of the polynomial ephemeris (Hilditch 2001),

$$(\mathrm{O-C}) = T_{\mathrm{ep}}(l) - t_0 - l P_{\mathrm{bin}} - \beta l^2 = \tau(t_l, K_{1,2}, P_{1,2}, e_{1,2}, \omega_{1,2}, T_{1,2}). \tag{11}$$

The quantity β in equation (11) is a factor that describes the binary period damping (change) due to the mass transfer, magnetic braking, gravitational radiation and/or influence of a very distant companion:

$$\beta = \frac{1}{2} P_{\mathrm{bin}} \dot{P}_{\mathrm{bin}}.$$

Let us note that β should also be fitted simultaneously with other free parameters of the model. In the rest of this paper, we use a common notation in the extrasolar planets literature, that enumerates the planets by subsequent letters, i.e. ‘b’ ≡ ‘1’, ‘c’ ≡ ‘2’, etc., to avoid any confusion.

2.3 Newtonian model of the LTT effect

A derivation of the N-body model of the LTT is basically very simple. It requires the computation of the planetary contribution τ to the (O–C) signal through the numerical integration of the equations of motion, a computation of the star barycentric vector $\boldsymbol{R}_*$ and its Z_* component, in accord with equation (5). This formulation accounts for the mutual interactions between all bodies in the system. A serious computational drawback of this model is a significant CPU overhead, nevertheless, as we will show in Appendix A, its application for systems with massive companions presumably involved in low-order MMRs can be indispensable, To solve the equations of motion efficiently, we used the ODEX2 integrator (Hairer, Nærsett & Wanner 2009) designed for conservative, second-order ordinary differential equations (ODEs). The imposed variable time-step accuracy preserved the total energy and the angular momentum better than 10^{-11}. In terms of the Newtonian model, the planetary bodies are parametrized through the mass m_i, semimajor axis a_i, eccentricity e_i and three Keplerian angles describing the orientation of the orbit, for each companion in the system. We also assume that the binary is a point mass with the prescribed total mass of the binary. Assuming a coplanar configuration (in the N-body model the same inclinations are 'absorbed' in the planetary masses), we have five free orbital parameters for each planet, similar to the kinematic model. Here, they are then represented as 'usual' osculating, astrocentric Keplerian elements at a given initial epoch, but other types of the osculating elements may be used as well.

2.4 The optimization method and numerical set-up

Having the egress times measured with a great precision (at the 1 s level, or even better), the next step is to determine the set of primary parameters of the kinematic model, usually with the least-squares approach, by constructing the reduced $(\chi^2_\nu)^{1/2}$-squared function:

$$(\chi^2_\nu)^{1/2} \equiv (\chi^2_\nu)^{1/2}(K_{1,2}, P_{1,2}, e_{1,2}, \omega_{1,2}, T_{1,2}, t_0, P_{\rm bin}, \beta),$$

and searching for its minimum in the space of the model parameters. It is well known, however, that the $(\chi^2_\nu)^{1/2}$ function may possess many local minima, particularly if the model is not well constrained, as it might be in our case. To seek a global solution, we apply a hybrid algorithm that consists of two steps: a quasi-global method, the genetic algorithm (GA; Charbonneau 1995) that is relatively slow and inaccurate, but makes it possible to find good approximations to the second step, a fast local method. Here, we use the Levenberg–Marquardt (L–M) algorithm with analytically computed derivatives. The idea of the hybrid code comes from our earlier works on modelling radial velocity observations (e.g. Goździewski & Konacki 2004). We used freely available FORTRAN codes of the GA (PIKAIA[1] by Phil Charbonneau and Barry Knapp) and of the L–M method from the well known MINPACK[2] package.

Once the primary set of the orbital model parameters are determined in the form of two five-tuples (K_i, P_i, e_i, ω_i, T_i), $i = 1, 2$, we may also derive inferred Keplerian elements, such as *minimal* planetary masses and semimajor axes, by solving non-linear equations expressing K_i (equations 7 and 8) and the third Kepler law in terms of the primary model parameters. The inclination has to be held fixed. Hence usually one assumes $i_i = 90^\circ$. Let us underline that while the LTT model (equation 9) formulated in the barycentre frame has the same mathematical form as in the Jacobi frame, the orbital, geometrical (Keplerian) elements in multiple systems should be related to Jacobian, canonical coordinates. If in the N-body numerical integrations and stability studies, initial conditions have to be in the form of osculating elements, one should transform these Jacobian elements into the Cartesian coordinates with respect to the Jacobi frame (e.g. Morbidelli 2002), and then, if necessary, to the astrocentric or barycentric coordinates. In this sense, 'barycentric' and 'Jacobian' two-body elements may closely coincide for small, Jovian-mass planets. But for more massive companions when the LTT signal is easier to detect, or for very compact (resonant) systems, the semimajor axes, masses, Keplerian angles and inferred N-body initial conditions may be significantly different in both frames. We will discuss this issue in more detail in a forthcoming article (Gozdziewski et al., in preparation).

Each run of the hybrid code has been initiated by random selection of the GA population (between 512 and 4096 individuals), considering possibly wide parameter ranges. For instance, the range of orbital periods was set blindly to [800, 63600] d, and angles and eccentricities were set to their whole possible ranges. The original 'population' was then transformed by GA operators over 512–1024 generations. Each member of the final set was then used as an initial condition for the L–M algorithm, and the resulting solutions were sorted and stored. The hybrid procedure was repeated hundreds of times for each combination of model-data set. We examined whether the obtained solutions converged to the same minima. Because of the semideterministic nature of the GAs, one should interpret the results in a statistical sense.

The same procedure may be applied to the Newtonian model, as the planetary contribution τ can be computed independently of the optimization method. (In this case the derivatives to the LM algorithm were approximated numerically.)

Finally, uncertainties of the best-fit parameters were determined using the bootstrap algorithm (Press 2002) as the variances of parameters in the tested solution that has been re-fitted to 4096 synthetic data sets drawn randomly with replacement from the original sample. We found that due to the particular distribution of OPTIMA observations that are grouped in small 'clumps' of a few data points, the bootstrap algorithm tends to underestimate the uncertainties when compared to the formal error determination through the diagonal elements of $(\chi^2_\nu)^{1/2}$ curvature (covariance) matrix.

3 KINEMATIC MODELLING THE LITERATURE DATA

To verify the literature models of the HU Aqr system, we gathered Barycentric Julian Date (BJD) egress times published by Schwope et al. (2001), Schwarz et al. (2009) and Qian et al. (2011). That data set consists of 113 points, and will be called the SSQ set hereafter. Our first attempt was to reproduce the results of Qian et al. (2011) with our formulation of the LTT model. We did not expect this to be straightforward, since their model assumes the inner planet to be on a circular orbit. We conducted calculations for two ephemeris models, linear and quadratic (equations 10 and 11), respectively.

3.1 The linear kinematic ephemeris two-planet model

In the linear ephemeris case, we found many, almost equally good two-planet solutions with $(\chi^2_\nu)^{1/2} \sim 1.15$ and an rms ∼2.3 s. In these best fits the inner planet has a period of ∼5500–6000 d. However, the period of the outer planet varies between 7000 and 20 000 d. The resulting systems imply (O–C) residuals caused individually by the

[1] http://www.hao.ucar.edu/modeling/pikaia/pikaia.php
[2] http://www.netlib.org/minpack/

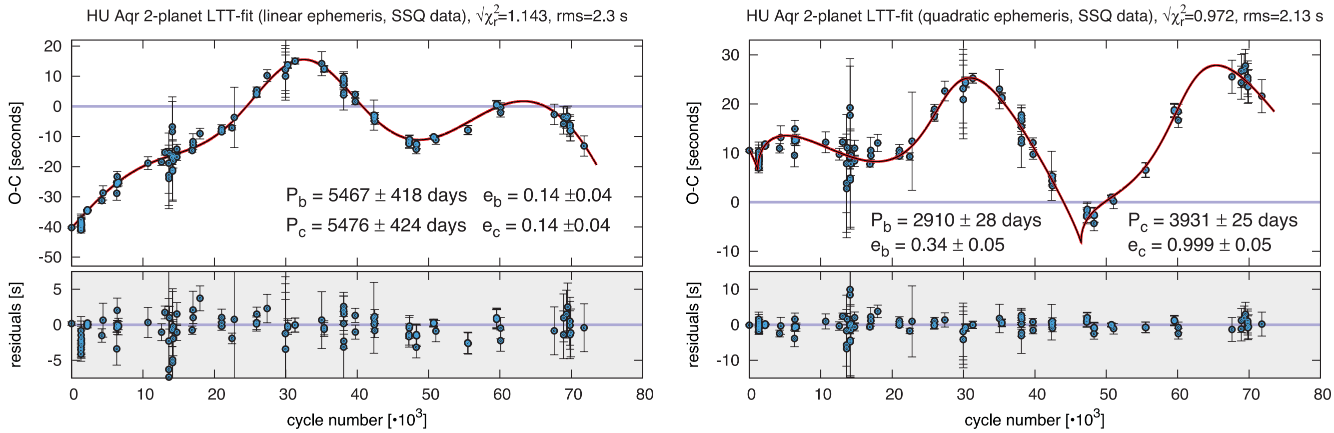

Figure 2. Synthetic curves of the best-fit, two-planet solutions to the mid-egress BJD times of the SSQ data set. The left-hand panel corresponds to a linear ephemeris model (equation 10) and the right-hand panel corresponds to a quadratic (parabolic) ephemeris model (equation (11), the parabolic trend has been removed). Panels are labelled with the orbital periods and eccentricities of the putative companions. Bottom plots with shaded background show the residuals after subtracting planetary and astrophysical contributions from the LTT signal. Discontinuous-like features of the parabolic ephemeris model around cycles 0 and 46 000 appear due to the extreme eccentricity of the outer body. See Table 1 for the orbital and inferred elements (Fits A and B, respectively).

Table 1. Jacobian geometric parameters with the inferred masses and semi-major axes of two-planet LTT fit models *in the barycentre frame* with the linear and parabolic ephemeris to the SSQ data set. Synthetic curves with data sets are shown in two panels of Fig. 2 and $(\chi^2_\nu)^{1/2}$ scans in Fig. 3. Numbers in parentheses represent the uncertainties at the last significant digit. Total mass of the binary is 1.08 $M_\odot$ (Schwarz et al. 2009). Indices 'b' and 'c' refer here to planets '1' and '2' in the mathematical model equations (10) and (11). See the text for more details.

Model parameter	Fit A linear ephemeris	Fit B parabolic ephemeris
K_b (s)	5928 ± 15	10.2 ± 0.5
P_b (d)	5467 ± 418	2910 ± 28
e_b	0.138 ± 0.034	0.34 ± 0.07
ω_b (°)	207 ± 21	22 ± 8
T_b (BJD 244 0000+)	11694 ± 175	5652 ± 97
K_c (s)	5942 ± 17	322 ± 30
P_c (d)	5476 ± 424	3931 ± 50
e_c	0.141 ± 0.035	0.99 ± 0.05
ω_c (°)	27 ± 20	358 ± 9
T_c (BJD 244 0000+)	6214 ± 451	9207 ± 42
P_bin (d)	0.086820400(4)	0.0868204250(8)
T_0 (BJD 244 0000+)	9102.92004(2)	9102.91988(2)
β ($\times 10^{-13}$ d cycle^{-2})	–	−3.06(6)
a_b (au)	1.375	4.08
$m_\mathrm{b} \sin i$ (M_Jup)	9780	5.69
a_c (au)	1.374	4.58
$m_\mathrm{c} \sin i$ (M_Jup)	9811	159
N	113	113
$(\chi^2_\nu)^{1/2}$	1.143	0.972
rms (s)	2.31	2.13

planets in wide ranges, up to ~6000 s, and companions in basically any mass, eccentricity and period range while still preserving excellent rms ~2.3 s and similar 'flat' behaviour of the residuals. The left-hand panel of Fig. 2 shows the most exotic and actually the best-fit solution found in our experiment. The Keplerian fit parameters of this solution, as well as its inferred elements are given in Table 1 (Fit A). This fit is very different from those found by Qian et al. (2011), Wittenmyer et al. (2012) and even in the last paper by Hinse et al. (2012). This configuration has $(\chi^2_\nu)^{1/2} \sim 1.143$ and an rms ~2.3 s, and is characterized by *almost equal* orbital periods of ~5470 d. The pericentre arguments of the planets in this fit differ by nominal value of 180°.2 and as a result, the Keplerian barycentric orbits are almost exactly anti-aligned, with planets placed close to their periastrons at the initial epoch. This configuration could be understood as a pair of *Trojan planets* in 1c:1b MMR. Although the resulting LTT signal has apparently small amplitude ~60 s as shown in the (O–C) diagram (see the left-hand panel in Fig. 2), the LTT semi-amplitudes $K_{\mathrm{b,c}}$ are excessively large (up to ~6000 s), implying just absurdly massive companions of ~10 000 Jupiter mass each (~10 $M_\odot$!). This solution reveals that an inherent degeneracy of the LTT signal (and its model) may appear because the signal is the result of the *differential* gravitational tugs of the companions on the binary. Indeed, in this particular Trojan configuration, even small deviations from the anti-alignment of orbits leads to large changes in the planetary masses (over three orders of magnitude) and semimajor axes (within a range of a few au), indicating that as they are not supported by the currently available observations, these dynamical parameters are poorly constrained. The mathematical fit permits putative companions as massive as stars. But in reality, such objects should influence dynamical and spectral properties of the binary system. Such solutions are therefore excluded.

The 1c:1b MMR solution is a vivid example demonstrating that due to the possibility of configurations involved in extremely strong mutual interactions, modelling the LTT signal globally (without any a priori assumptions on the system configuration) cannot be studied in terms of the kinematic model. In general, an exact, self-consistent N-body model should be used to determine the initial conditions.

3.2 The quadratic kinematic ephemeris two-planet model

In the case of a quadratic ephemeris, we found a well defined minimum of $(\chi^2_\nu)^{1/2} \sim 0.972$, which is an apparently statistically perfect solution. Its synthetic curve with measurements overplotted is shown in the right-hand panel of Fig. 2, and orbital parameters are given in Table 1 as Fit B. That solution has been frequently found in different runs of the hybrid code, which reinforces its global character. To show the latter, we computed parameter scans of $(\chi^2_\nu)^{1/2}$ in the $(P_{\mathrm{b,c}}, e_{\mathrm{b,c}})$ planes (Fig. 3), by fixing points of a grid in a given

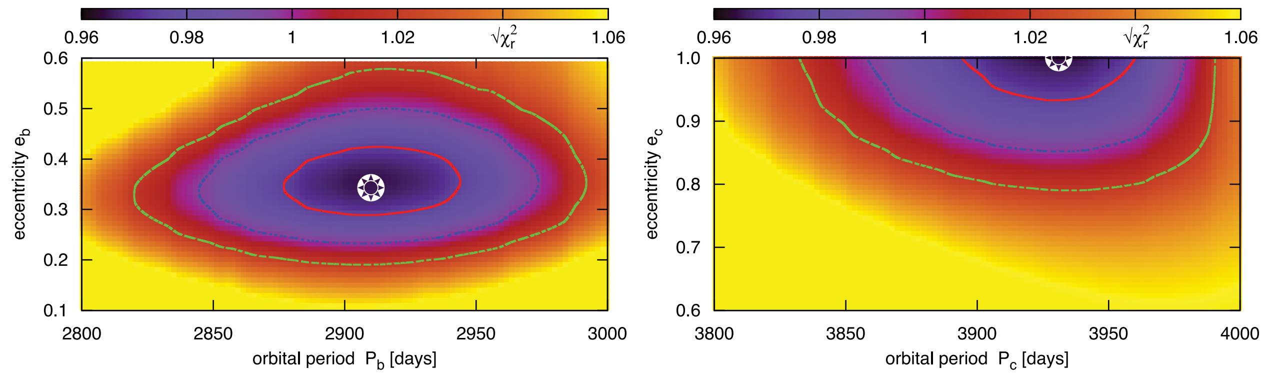

Figure 3. Parameter scans of the $(\chi_\nu^2)^{1/2}$ function computed around the best-fit solution to the SSQ data for the quadratic ephemeris model (see the right-hand panel in Fig. 2 and Fit B in Table 1). Colour curves are for the formal 1, 2, 3σ levels of the best-fit solution whose parameters are marked with an asterisk.

plane and minimizing $(\chi_\nu^2)^{1/2}$ over all remaining free parameters of the model. This made it possible to obtain standard confidence levels as marked with coloured curves. The best-fit solution is again very different from solutions found in the literature. While the elements of the inner planet are well constrained, the orbit of the outermost companion reveals extremely large eccentricity ($\sim$1). That points again to highly degenerate (unrealistic) best-fit solutions, with near-parabolic or even hyperbolic, open orbit of one 'planet' – as the fit implies – being a low-mass stellar object of $\sim$160 Jupiter masses. Other solutions with slightly worse $(\chi_\nu^2)^{1/2} \sim 1.1$ and still very similar rms $\sim$2.2 s may be found too, which means that the quadratic ephemeris model is unconstrained by the SSQ data.

In the quadratic ephemeris model, the orbital periods are close to the 4:3 ratio, which is equivalent to the low-order 4c:3b MMR. In addition, the eccentricity of the outer planet is extreme, close to 1. Hence again, the kinematic formulation seems inadequate to derive the proper initial condition of the multiple-planet configuration. We conclude here that when we only have the SSQ data at our disposal, there seems to be no unique and physically meaningful solution explaining the LTT variability. Or, the planetary fit model and its assumptions are incorrect.

4 NEW OBSERVATIONS AND DATA REDUCTION

4.1 Observations with OPTIMA and other instruments

To resolve the model degeneracies as described above, we gathered new, yet unpublished observations of the HU Aqr binary. The new collected mid-egress BJD times are given in Table 2. These data extend the work of Schwope et al. (2001), Schwarz et al. (2009) and Qian et al. (2011). The currently available data set of HU Aqr egress times consists of 171 measurements in total, including 10 points presented in Qian et al. (2011). Among these measurements, 68 were obtained with the OPTIMA instrument that operates mostly at the 1.3-m telescope at Skinakas Observatory, Crete, Greece.

The high-speed photometer OPTIMA is a sensitive, portable detector to observe extremely faint optical pulsars and other highly variable astrophysical sources. The detector contains eight fibre-fed single photon counters – avalanche photodiodes (APDs), and a GPS for the time control. There are seven fibres in the bundle (Fig. 4) and one separate fibre located at a distance of $\sim$1 arcmin. Single

Table 2. New HU Aqr BJD mid-egress times on the basis of light curves collected with OPT-ESO22 – OPTIMA photometer installed at ESO (Chile), OPT-SKO – OPTIMA operated at the Skinakas Observatory (Crete), PIRATE – a telescope at the Astronomical Observatory of Mallorca, MONET/N – the network of telescopes at the McDonald Observatory, and the SAO (South Africa) and WFC – the 1.5-m TCS (Canary Islands). The first 58 data points are not yet published. The remaining 21 mid-egress times are re-computed from archival OPTIMA light curves in Schwarz et al. (2009). See the text for details.

Cycle	BJD	Error (d)	Instrument
29 946	245 1702.8443352	0.000 0037	OPT-ESO22
29 957	245 1703.7993545	0.000 0038	OPT-ESO22
29 958	245 1703.8861705	0.000 0034	OPT-ESO22
30 265	245 1730.5400324	0.000 0041	OPT-SKO
30 287	245 1732.4500902	0.000 0023	OPT-SKO
30 299	245 1733.4919357	0.000 0033	OPT-SKO
30 300	245 1733.5787554	0.000 0054	OPT-SKO
30 310	245 1734.4469740	0.000 0031	OPT-SKO
30 311	245 1734.5337856	0.000 0018	OPT-SKO
35 469	245 2182.3533852	0.000 0030	OPT-SKO
38 098	245 2410.6041626	0.000 0084	OPT-SKO
42 486	245 2791.5719484	0.000 0015	OPT-SAO
42 487	245 2791.6587715	0.000 0024	OPT-SAO
44 534	245 2969.3800760	0.000 0033	OPT-NOT
44 557	245 2971.3769377	0.000 0085	OPT-NOT
51 020	245 3532.4971595	0.000 0100	OPT-SKO
51 066	245 3536.4909030	0.000 0064	OPT-SKO
51 067	245 3536.5777278	0.000 0033	OPT-SKO
55 535	245 3924.4913426	0.000 0102	OPT-SKO
55 627	245 3932.4788164	0.000 0061	OPT-SKO
55 661	245 3935.4307071	0.000 0064	OPT-SKO
55 719	245 3940.4662754	0.000 0162	OPT-SKO
60 085	245 4319.5242409	0.000 0074	OPT-SKO
64 657	245 4716.4671496	0.000 0053	OPT-SKO
64 885	245 4736.2622085	0.000 0038	OPT-SKO
64 886	245 4736.3490181	0.000 0016	OPT-SKO
65 265	245 4769.2539926	0.000 0023	OPT-SKO
67 791	245 4988.5622710	0.000 0029	OPT-SKO
67 917	245 4999.5016391	0.000 0017	OPT-SKO
67 918	245 4999.5884526	0.000 0054	OPT-SKO
68 009	245 5007.4891162	0.000 0018	OPT-SKO
72 099	245 5362.5844371	0.000 0032	OPT-SKO
72 110	245 5363.5394546	0.000 0019	OPT-SKO
72 121	245 5364.4944885	0.000 0029	OPT-SKO
72 133	245 5365.5363444	0.000 0015	OPT-SKO
72 225	245 5373.5238044	0.000 0048	OPT-SKO

Table 2 – *continued*

Cycle	BJD	Error (d)	Instrument
72 237	245 5374.5656456	0.000 0040	OPT-SKO
72 248	245 5375.5206715	0.000 0040	OPT-SKO
72 305	245 5380.4694292	0.000 0030	OPT-SKO
72 351	245 5384.4631748	0.000 0024	OPT-SKO
72 352	245 5384.5499944	0.000 0022	OPT-SKO
72 421	245 5390.5406108	0.000 0013	OPT-SKO
73 409	245 5476.3190971	0.000 0578	PIRATE
73 559	245 5489.3421698	0.000 0578	PIRATE
73 560	245 5489.4290151	0.000 1156	PIRATE
75 467	245 5654.9954277	0.000 0040	MONET/N
75 812	245 5684.9484608	0.000 0023	MONET/N
76 721	245 5763.8681410	0.000 0035	MONET/N
77 031	245 5790.7824571	0.000 0039	MONET/N
77 066	245 5793.8211556	0.000 0077	MONET/N
77 067	245 5793.9079841	0.000 0055	MONET/N
77 078	245 5794.8630179	0.000 0065	MONET/N
77 546	245 5835.4949490	0.000 0179	WFC
77 557	245 5836.4499905	0.000 0295	WFC
77 789	245 5856.5922852	0.000 0038	MONET/N
77 802	245 5857.7209399	0.000 0090	MONET/N
77 823	245 5859.5441786	0.000 0066	MONET/N
78 100	245 5883.5934038	0.000 0022	MONET/N
30276	245 1731.4950648	0.0000017	OPT-SKO
30277	245 1731.5818971	0.0000019	OPT-SKO
35376	245 2174.2790965	0.0000018	OPT-SKO
35377	245 2174.3659101	0.0000022	OPT-SKO
38109	245 2411.5591932	0.0000034	OPT-SKO
42441	245 2787.6650399	0.0000015	OPT-SAO
42463	245 2789.5750934	0.0000014	OPT-SAO
42464	245 2789.6619272	0.0000024	OPT-SAO
47253	245 3205.4447079	0.0000027	OPT-SKO
47254	245 3205.5315288	0.0000037	OPT-SKO
47300	245 3209.5252729	0.0000038	OPT-SKO
47335	245 3212.5640023	0.0000038	OPT-SKO
48265	245 3293.3069570	0.0000102	OPT-SKO
48288	245 3295.3038228	0.0000035	OPT-SKO
48299	245 3296.2588336	0.0000066	OPT-SKO
48334	245 3299.2975567	0.0000015	OPT-SKO
51032	245 3533.5390170	0.0000052	OPT-SKO
55466	245 3918.5007189	0.0000046	OPT-SKO
55546	245 3925.4463562	0.0000075	OPT-SKO
60096	245 4320.4792541	0.0000037	OPT-SKO
60097	245 4320.5660769	0.0000055	OPT-SKO

photons are recorded simultaneously and separately in all channels with absolute UTC time-scale tagging accuracy of ~4 μs. The quantum efficiency of the APDs reaches a maximum of 60 per cent at 750 nm and lies above 20 per cent in the range 450–950 nm (Kanbach et al. 2003, 2008). During the HU Aqr observations, OPTIMA was pointed at RA(J2000) = $21^{\rm h}07^{\rm m}58^{\rm s}.19$, Dec.(J2000) = $-05^\circ17'40''.5$, corresponding to the central aperture of the fibres bundle (Fig. 4). For sky background monitoring, we usually choose one out of the six hexagonally located fibres. We look for the fibre that is not by chance pointed to any source, therefore records sky background, and its response is the most similar to the central fibre response when the instrument is targeted at the dark sky. An example of a sky background subtracted light curve is shown at the top left-hand panel in Fig. 5.

We derived new fits to the HU Aqr eclipse egress times, as well as reanalysed many of the already published OPTIMA data. There are 26 eclipses obtained by OPTIMA published by Schwarz et al. (2009). We were able to reanalyse only 21 out of the 26 light curves, because only those were available in the OPTIMA archive. Our completely new data set includes 42 precision photometric observations, starting from cycle $l \sim 29\,900$, overlapping in time window with the literature data. We derived 23 new eclipse profiles from the OPTIMA data archive spanning 1999–2007 and obtained 19 new OPTIMA optical HU Aqr light curves in 2008–2010. Note that some of the OPTIMA observations have been already published in the very recent literature (Nasiroglu et al. 2010).

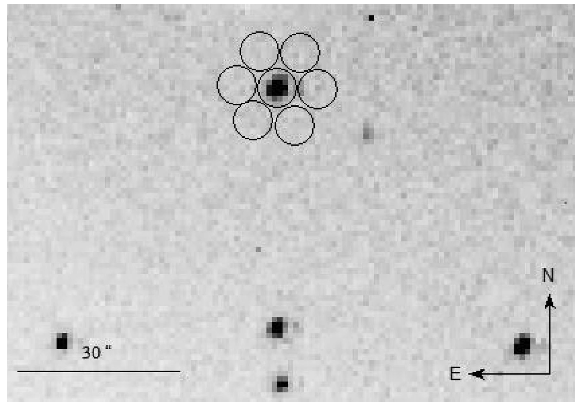

Figure 4. OPTIMA hexagonal fibre bundle centred on HU Aqr. The ring fibres (1–6) are used to monitor the background sky simultaneously.

We also gathered and reduced 11 observations performed at the MONET project which is a network of two 1.2-m telescopes operated by the Georg-August-Universität Göttingen, the McDonald Observatory and the South African Astronomical Observatory. These precision data in white light (500–800 nm) were binned in 5 s intervals, with 10^{-6} d (0.1 s) accuracy, separated by 3 s readout. The most recent observations were performed on 2011 November 18.

An additional three egress times were obtained from the eclipse observations carried out with the PIRATE telescope equipped with the SBIG STL1001E CCD camera (Holmes et al. 2011). PIRATE, funded by the Open University, Department of Physics and Astronomy, is a remote-controlled telescope located at the Astronomical Observatory of Mallorca (OAM), Spain.

We also performed optical observations of HU Aqr in white light with the 1.5-m TCS equipped with Wide FastCam (WFC; Fig. 6). The WFC is a 1k × 1k pixel camera with optics offering a field of view (FOV) of 12 arcmin with a scale of 0.6 arcsec pixel^{-1}. HU Aqr eclipses were observed on 2011 September 30 and October 1 with integration times of 3 and 5 s, respectively. WFC works in frame transfer mode, therefore, the readout time is effectively null or in other words is equivalent to the exposure time. UTC mid-exposure times of the photometric measurements were converted to the BJD in Barycentric Dynamical Time using the procedure developed by Eastman, Siverd & Gaudi (2010).

Some technical details of the observations performed with the MONET/N, TCS and PIRATE telescopes are given in Table 3.

4.2 Determining time markers of the eclipses

In Fig. 5 we show an example of HU Aqr high time resolution OPTIMA photometric (see the right-hand top panel, and blue curve in the left-hand top panel) and polarimetric (Stokes I, red curve in the right-hand top panel) light curves. These graphs are to be compared with the light curves from TCS, obtained with 3 and 5 s exposures illustrated in Fig. 6. Obviously, the OPTIMA resolution

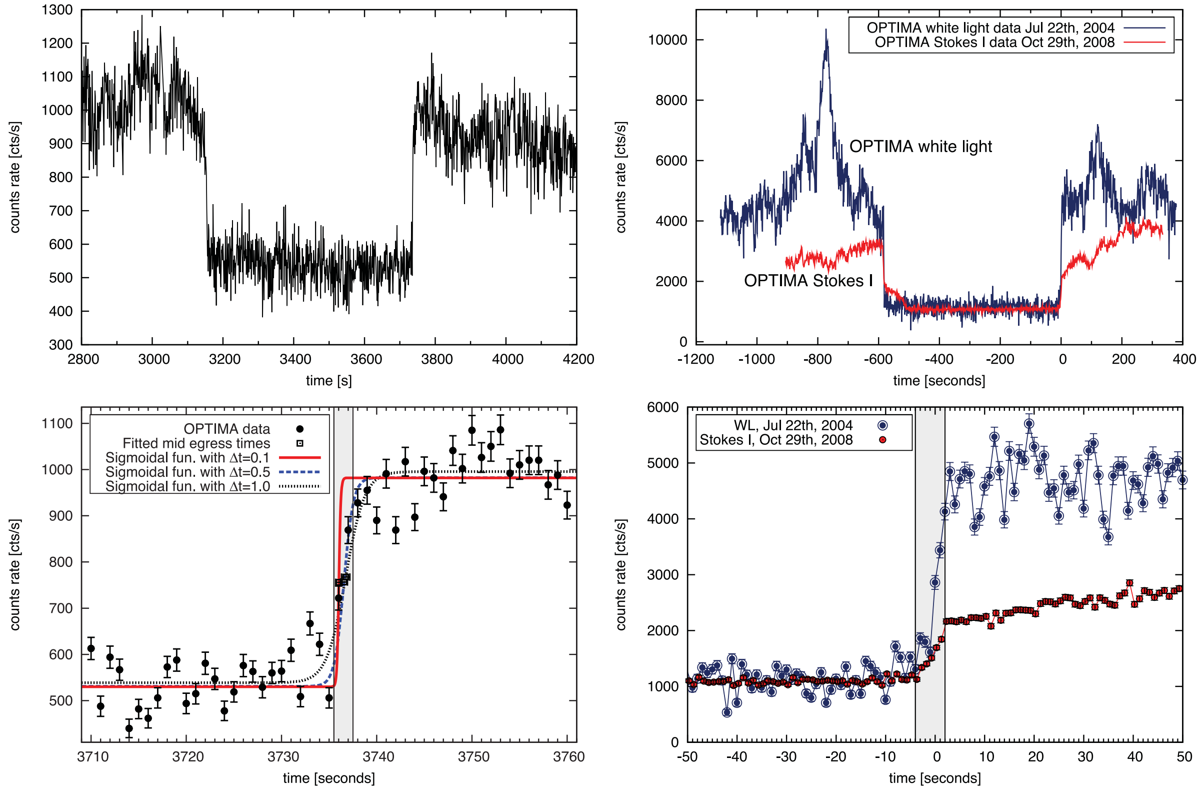

Figure 5. High time resolved OPTIMA light curves of HU Aqr. Upper left-hand panel: photometric eclipse in the white light. Bottom left-hand panel: a close-up around the mid-egress overplotted with three fitted sigmoid functions with different values set for the Δt parameter (0.1, 0.5, 1.0, respectively). The fitted mid-egress times are denoted by open squares. The shaded region corresponds to a time-span of 2 s. Upper right-hand panel: a comparison of photometric and polarimetric OPTIMA light curves of HU Aqr obtained in 2004 and 2008, respectively. Bottom right-hand panel: a close-up of photometric and polarimetric HU Aqr light curves around the mid-egress time showing the difference between the egress shapes. The shaded region covers 6 s.

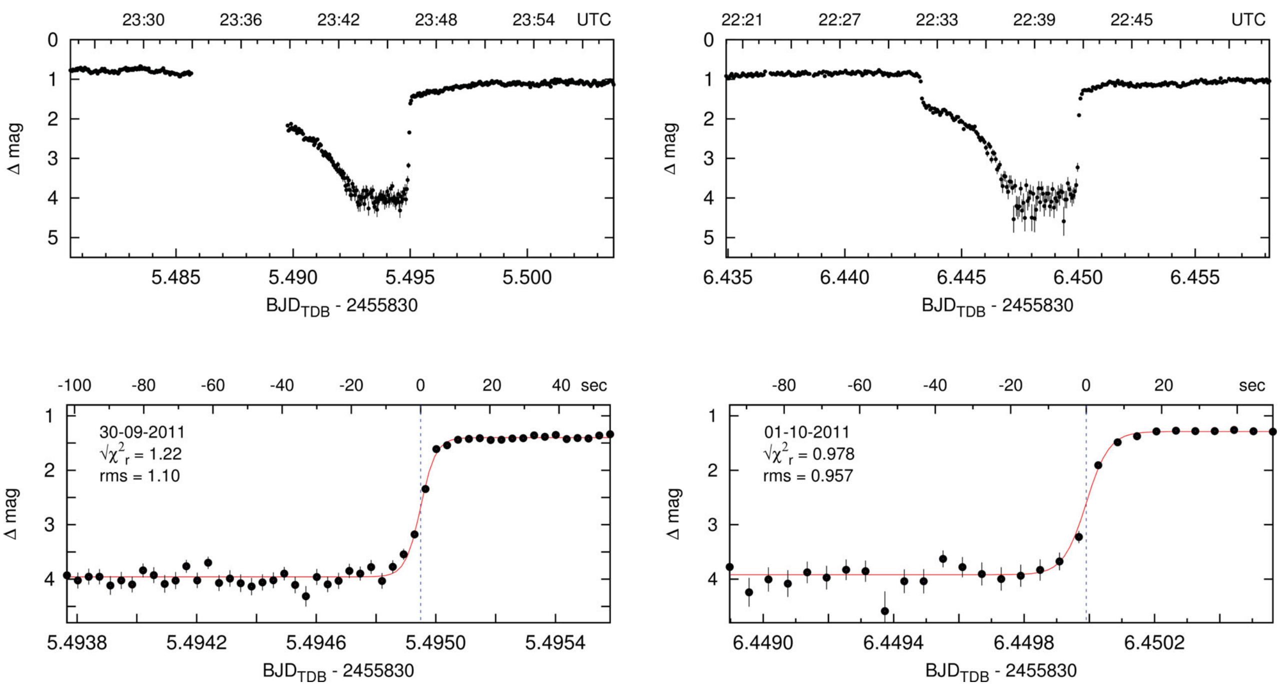

Figure 6. HU Aqr eclipse light curves obtained with the WFC mounted on the TCS. Observations were performed on 2011 September 30 and October 1 with integration times of 3 and 5 s, respectively. Bottom panels are for the close-up of eclipse egress, with fitted sigmoid function (solid line, see equation 12). Blue vertical lines mark the determined mid-egress times.

Table 3. Technical data of the MONET/N, PIRATE and TCS observations of HU Aqr. $T_{\rm obs}$ represents the observation time-span, and ΔT is the mean exposure time of a single frame.

Date	Instrument	Filter	$T_{\rm obs}$ (h)	ΔT (s)
2010 October 6	PIRATE	*WL*	1	10
2010 October 19	PIRATE	*WL*	3.5	10, 20
2011 September 30	TCS/WFC	*WL*	1	3
2011 October 1	TCS/WFC	*WL*	1	5
2011 April 3	MONET/N	*WL*	0.60	8
2011 May 3	MONET/N	*WL*	0.50	8
2011 July 21	MONET/N	*WL*	0.32	8
2011 August 17	MONET/N	*WL*	0.60	8
2011 August 20	MONET/N	*WL*	0.46	8
2011 August 20	MONET/N	*WL*	0.10	8
2011 August 21	MONET/N	*WL*	0.58	8
2011 October 22	MONET/N	*WL*	0.25	8
2011 October 23	MONET/N	*WL*	0.50	8
2011 October 25	MONET/N	*WL*	0.16	8
2011 November 18	MONET/N	*WL*	0.45	8

makes it possible to track the egress phase closely, which enabled us to determine the mid-egress moments very precisely.

Measuring the time of mid-egress properly is critical to obtain the (O–C) diagrams, since it is the time marker of the eclipse (Schwope et al. 2001; Schwarz et al. 2009). To derive the mid-egress moment t_0, the sigmoid function,

$$I(t) = a_1 + \frac{(a_2 - a_1)}{(1.0 + \exp([t_0 - t]/\Delta t)}, \quad (12)$$

parametrized by a_1, a_2 and t_0 was fitted to the light-curve points in the egress phase of the eclipse, spanning pre-selected exponential scaling parameters Δt. We found that there is no strong dependence of the derived t_0 on the adopted Δt. This can be seen in the bottom left-hand panel of Fig. 5 where three mid-egress times t_0 are marked with black open squares. These moments are derived for three different choices of Δt: 0.1, 0.5 and 1.0, respectively. While these times depend on Δt, they fall within a 2 s range, as marked by a shaded strip at the bottom left-hand panel of Fig. 5. A half of that range ($\sim$1 s) may be typically estimated as the maximum possible error of t_0 in the OPTIMA data set. The formal 1σ uncertainty of the sigmoid fit in this case is still smaller and at the level of $\sim$0.1 s. Moreover, the shape of the eclipse may significantly depend on the spectral window. Panels in the right-hand column of Fig. 5 illustrate the light curves of HU Aqr derived in the optical, white band domain (the blue curve) and in the polarimetric domain (Stokes I, the red curve). In the latter case, the egress looks quite different and spans over a longer time. Given that these two data sets were taken 4 yr apart, the observed difference might have been caused by different emission states of the source. To derive the mid-egress moments gathered in Table 2, the sigmoid function was fitted to all single light curves.

4.3 On the light curves in different spectral windows

Vogel et al. (2008) and Vogel (2008) obtained high time resolved and accurate light curves of HU Aqr during its low state using the ULTRACAM (Beard et al. 2002; Dhillon et al. 2007) at the Very Large Telescope (VLT; 2005 May 13). These authors decomposed the light curve into three emission components emerging from the accretion spot, the photosphere surrounding it and from the WD itself. As a result, they were able to derive the temperature of the WD $\sim$ 13 500(200) K and the temperature of the accretion spot $\sim$25 500(1500) K. They also estimated the ratio of the spot area to the WD surface to be on the level of 5 per cent. The blackbody spectra of the WD and of the spot have their maxima at 215 and 113 nm, respectively. The accretion spot and the accretion stream are time variable in brightness, as well as in the geometric position in the system. Therefore, the orbital phase at which they occur is not constant. The ULTRACAM delivers simultaneous light curves in three colours: u, g and r. An example of such a three-colour HU Aqr light curve can be found in fig. 6 of Schwarz et al. (2009), where the shape–energy dependence can be easily seen. Thus, a comparison of egress times in different wavelength domains was possible. In the two cases with filters u and r, the WD constitutes the main contribution to the egress intensity, because it can be seen unperturbed when it comes out of eclipse. However, during high and intermediate accretion states, the WD might be out-shined by the accretion stream. In the u band, the spot contributes 25 per cent of the emission, while in the r band its contribution is only 12 per cent (Vogel 2008; Vogel et al. 2008). This suggests that as the time marker of the eclipse, it is better to use more 'reddish' than 'bluish' data, particularly in our case as we have broad-band observations gathered in X-rays, UV and optical domains at our disposal.

There exists evidence that the *Extreme Ultraviolet Explorer* (*EUVE*) light curves differ from quasi-simultaneous *ROSAT*/High Resolution Imager (HRI) light curves, as it can be seen, for example, for eclipses recorded on 1996 October and 1997 May, as shown in fig. 2 of Schwope et al. (2001). The eclipse ingress is often not measured because of strong suppression of soft X-rays by absorbing matter along the accretion stream. When the eclipse duration can be determined, the eclipse duration seems shorter in the case of *EUVE* data. Thus the derived mid-egress moments can be shifted by a few seconds. According to Schwope et al. (2001), an expected variation of the eclipse span should be not more than 0.001 of the orbital phase which corresponds to not more than $\sim$8 s. Also Schwope et al. (2004) show in their fig. 3 evidence of a different eclipse length as well as phase folded egress shapes at soft X-rays, *Hubble Space Telescope* (*HST*) UV and high-speed optical photometry with a multichannel multicolour photometer (the MCCP 2.2-m telescope at Calar Alto) during the 1993 high state and the 1996 low accretion state. The scatter of the egress times resulting from changes of the accretion geometry during high and intermediate accretion states is estimated on the level of 2 s (Schwarz et al. 2009). Large differences between light curves due to the eclipse of the accretion stream are also visible in the optical photometric measurements performed in parallel with the *ROSAT* observations (see fig. 3 in Schwope et al. 2001). Some of those light curves were obtained with rather poor time resolution, e.g. 53 and 12 s.

It is worth mentioning that time stamps calculated by Schwope et al. (2001) and Schwarz et al. (2009) for the photon counting UV and X–ray detectors were computed from the mean of the arrival times of the first three photons after the eclipse, while for the optical observations, they used the moments of the egress half-intensity, which is common in the literature. Examples of the HU Aqr light curves obtained by the *XMM–Newton* European Photon Imaging Camera (EPIC)-PN and Optical Monitor detectors are presented in figs 2–4 of Schwarz et al. (2009). *XMM* observations, contrary to the bright state *ROSAT* observations, were not resolved at time-scales shorter than 2 s due to the low count rates.

We first used all available egress times, archival as well as new ones, to model the (O–C) diagram. However, given the above-mentioned arguments, we decided to select only those measurements that were obtained in the white light or photometric V band, in order to keep the data more uniform and homogeneous. This

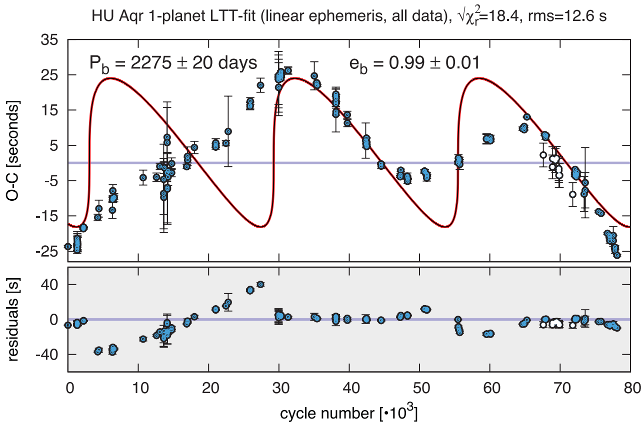

Figure 7. Synthetic curve of the one-planet LTT model with linear ephemeris to all available data, including the very recent egress times collected by the OPTIMA photometer, as well as PIRATE, TCS and MONET/N telescopes. Open circles are for measurements in Qian et al. (2011).

approach renders the measurements independent of possible varying emission regions in different bands. We also decided to skip the most 'suspicious' egress times at some stage of fitting the orbital model, which is described below.

We note that the *HST* observations (three points around $l \sim 14\,000$) were performed with the Faint Object Spectrograph (FOS) instrument in the 120–250 nm range. These points were also excluded in our further analysis, falling out of the white light and the V-band range.

5 MODELLING ALL RECENT DATA

Thanks to the new set of precision OPTIMA mid-egress measurements, as well as observations performed at PIRATE, TCS and MONET/N telescopes, we can re-fit planetary models to the whole set of data up to 2011 November 18. We fitted the data with the linear and quadratic ephemeris models (equations 10 and 11).

5.1 Single-planet models to all recent data

At the first attempt, we tested the one-planet hypothesis. For the linear ephemeris model, the one-planet solution is characterized by extreme eccentricity and displays large residuals and a strong trend present in the (O–C) diagram (see Fig. 7). This suggests a more general quadratic model, on which we focus now.

The results derived for the whole set of 171 measurements are shown in the top panels of Fig. 8. Interestingly, the one-planet model fits the data very well in a large part of the time window between $l = 25\,000$ and $80\,000$ (see the left-hand panel of Fig. 8). However, over approximately one-fourth of the time window ($l = 0$–$25\,000$), the data fit the synthetic curve poorly. That can be better seen in the close-up of the residuals shown in the top

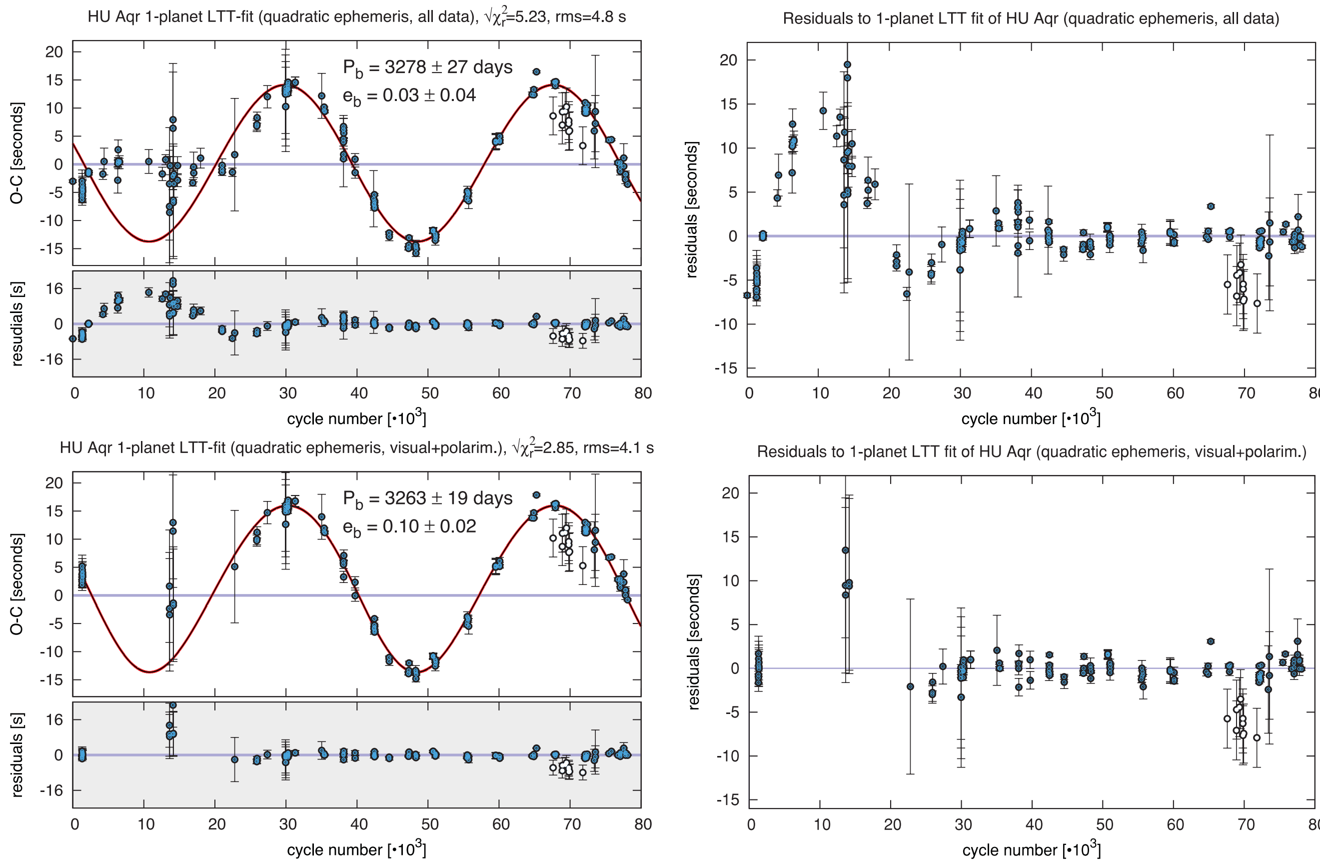

Figure 8. Top row: synthetic curve of the one-planet LTT model with quadratic ephemeris to all available data, gathered in this work, including the very recent mid-egress times collected by the OPTIMA photometer, as well as PIRATE, TCS and MONET/N telescopes (top left-hand panel) with orbital parameters given in Table 4 (Fit I), and close-up of residuals to that model (top right-hand panel). Bottom row: the same for the white light and visual band (V) data, including polarimetric observations by OPTIMA (i.e. the UV- and X-band observations are excluded) shown at the bottom left-hand panel, and its residuals (bottom right-hand panel). The white filled circles mark the Qian et al. (2011) measurements.

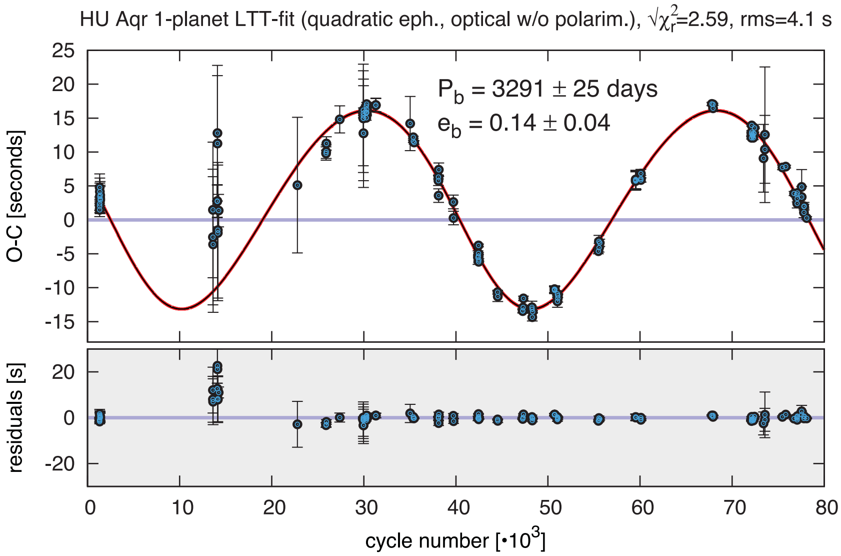

Figure 9. Synthetic curve of the one-planet LTT model with quadratic ephemeris to observations in white light + V band (see the text for more details) *without* measurements in Qian et. al (2011) and polarimetric data. Orbital parameters of this solution are given in Table 4 (Fit II).

right-hand panel of Fig. 8. It appears that the residuals follow a regular and characteristic 'damping' trend that could be associated with a mass-transfer process ongoing in the binary or solar-like magnetic cycles. Results of our experiments show that the recent observations by Qian et al. (2011) appear to be outliers to our one-planet solution, as the mid-egress times are shifted by about of 3–10 s with respect to the synthetic curve. Because these observations overlap in the time window with much more precise OPTIMA data, that discrepancy between these two data sets cannot be avoided. Actually, observations by Qian et al. (2011) do not fit any model that has been tested with the OPTIMA observations, including two-planet models and both types of the ephemeris (see Appendix A).

In an effort to explain the strange behaviour of the residuals, we realized, as it was discussed already, that the available observations come from different telescopes/instrumentation, and to make the matter worse, the egress times are measured on the basis of light curves in different spectral windows. In particular, the first part of the data set contains the egress times derived from X-rays (*ROSAT* and *XMM*) and ultraviolet (*EUVE*, *XMM* OM-UVM2 and *HST*/FOS) light curves, and some eclipses were observed with OPTIMA in polarimetric mode. To remove the possible inconsistency due to the different spectral windows and filters, we considered data sets consisting of the egress times measured only in the optical range (white light and the V band). The results are shown in the bottom panels of Fig. 8 for the optical data *without* X-ray and UV, but *including* polarimetric measurements (note that the polarimetry was done in the white-light band; compare with the top panels of Fig. 8 for all data gathered). As can be seen from the bottom panels in Fig. 8, the 'damping' effect has almost vanished, suggesting that it could have appeared due to the presence of X-ray and UV-derived eclipses. Still, there is a group of data points with large errors, around $l \sim 14\,000$, which do not fit well to the clear quasi-sinusoidal variation of the (O–C). The deviations of these points may be explained by poor time resolution (∼12 s of the AIP07 CCD camera), that has been used to observe the HU Aqr eclipses (Schwope et al. 2001). Let us also note that the Qian et al. (2011) data points are again systematically outliers with respect to the synthetic signal. After removing these data and all points (seven measurements) in the polarimetric mode, we obtained a homogeneous optical data set to which we fitted the quadratic ephemeris one-planet model again. The synthetic curve of this fit with data points overplotted is shown in Fig. 9. Parameters of this fit are presented in Table 4 as the final solution Fit II and are well constrained by the observations. To demonstrate the latter, we show projections of $(\chi^2_\nu)^{1/2}$ in selected two-dimensional parameter planes (see Fig. 10) close to the best-fit model. As can be seen, there is a strong correlation between the time and argument of pericentre which can be understood noting that the orbital phase ($\lambda_b = \varpi_b + M_b$) must be preserved.

The best-fit model seem to constrain the damping factor $\beta \sim -3 \times 10^{-13}$ d cycle^{-2} very well. Such a value is close to estimates in the literature, e.g. $\sim -5 \times 10^{-13}$ d cycle^{-2} by Schwarz et al. (2009) and $\sim -2.5 \times 10^{-13}$ d cycle^{-2} by Qian et al. (2011). It

Table 4. Keplerian parameters for the one-planet LTT fit model with quadratic ephemeris to all data gathered in this work (Fit I) and to measurements selected in the optical and V-band domain (Fit II). Synthetic curves with mid-egress times overplotted are shown in Figs 8 and 9. Numbers in parentheses represent the uncertainty at the last significant digit. Total mass of the binary is 0.98 $M_\odot$ (Schwope et al. 2011). See the text for more details.

Model parameter	Fit I all measurements	Fit II optical measurements
K_b (s)	13.9 ± 0.3	14.7 ± 0.2
P_b (d)	3278 ± 28	3287 ± 19
e_b	0.03 ± 0.04	0.13 ± 0.04
ω_b (°)	211 ± 40	226 ± 10
T_b (BJD 244 0000+)	6233 ± 360	6361 ± 102
P_{bin} (d)	0.0868204226(5)	0.0868204259(4)
T_0 (BJD 244 0000+)	9102.92004(2)	9102.91994(1)
β ($\times 10^{-13}$ d cycle^{-2})	−2.61 (5)	−2.95(4)
a_b (au)	4.29	4.30
$m_b \sin i$ (M_{Jup})	6.71	7.10
N data	171	115
$(\chi^2_\nu)^{1/2}$	5.23	2.48
rms (s)	4.8	3.7

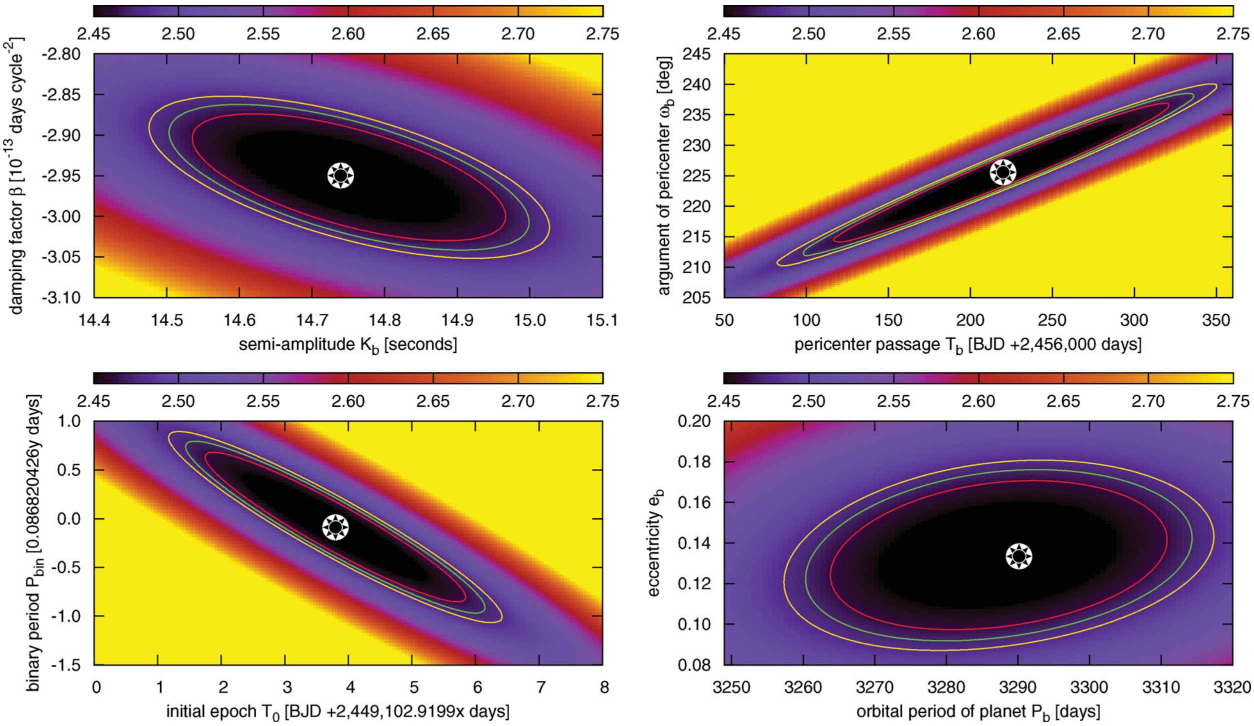

Figure 10. Colour-coded parameter scans of $(\chi_\nu^2)^{1/2}$ around the best-fit one-planet model, to quadratic ephemeris and the optical measurements (Fit II in Table 4). Its synthetic curve with data points overplotted is shown in Fig. 9. The large symbol marks nominal elements of the solution. Closed curves are for formal 1, 2, 3σ levels of $(\chi_\nu^2)^{1/2}$ with scale displayed at the colour legend.

is still larger by more than one order of magnitude to be explained by gravitational radiation, but remains in the range of magnetic braking (Schwarz et al. 2009). A similar large-magnitude period decrease has been found in other CVs, like NN Ser ($\sim -6 \times 10^{-13}$ d cycle^{-2}; Brinkworth et al. 2006). Besides the angular momentum loss, the large magnitude of the period change is commonly explained as due to the Applegate mechanism (basically excluded in the HU Aqr) and/or the presence of a very distant, long-period companion body. Likely, a few astrophysical and/or dynamical effects may be involved that could determine apparently secular period decrease. Its definite explanation is complex, and we consider this as a subject of a new, forthcoming work.

We also fitted the quadratic ephemeris model only to the highest precision OPTIMA data. The results for measurements that *include* polarimetric observations are shown in Fig. 11. For that case, we found a period similar to the quadratic ephemeris model for the entire data set. The fit has very small rms $\sim$0.8 s. The relatively large $(\chi_\nu^2)^{1/2} \sim 3.4$ of the OPTIMA solution in this case may suggest that the adopted uncertainties, at the $\sim$0.1–0.2 s level (in a large subset of the measurements) are in fact underestimated. We also identified the most deviating points as coming from the polarimetric measurements (see e.g. a point marked in the residuals plot around $l = 65\,000$, and the residuals of both solutions). To examine whether these data may change the solution, we fitted the quadratic ephemeris model to the white light OPTIMA observations only, skipping all polarimetric data. The best-fit orbital period of $\sim$3400 d remains close to the full-coverage window fit. A slightly smaller rms of $\sim$0.7 s suggests a better fit without the polarimetric data, indeed. The orbital periods coincidence cannot be fully proved due to the relatively narrow observational window of the OPTIMA white light measurements. Actually, the parameter scan (not shown here) reveals that the 1σ contour around the $(\chi_\nu^2)^{1/2}$ minimum in

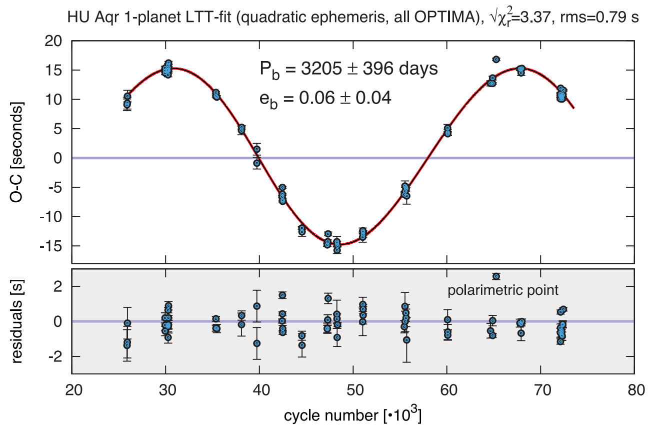

Figure 11. Synthetic curves of the one-planet LTT quadratic ephemeris models to optical OPTIMA measurements, including polarimetric data. One of the most deviating polarimetric points is labelled in the residuals panel.

the(P_b, e_b) plane is 'opened' on the right-hand side of the orbital period axis, hence it cannot be constrained yet by the OPTIMA data alone.

5.2 Alternate models to all recent data

Finally, using the hybrid optimizer, we performed additional experiments by fitting three models to all available data: the one-planet model with a heuristic sine damping term, and two-planet models, both in terms of the linear and quadratic ephemeris. We also performed N-body modelling of the two-planet configurations. The results, which are described in Appendix A, imply that all these models lead to non-unique solutions or configurations with similar orbital periods for which the kinematic model is inadequate, as we discussed above. Some of these kinematic best-fit two-planet solutions are qualitatively similar to configurations found for the SSQ data set, with orbital period ratios close to 1c:1b and 4c:3b, respectively. The extended data set still does not constrain the Keplerian two-planet models.

The same can be concluded for the *N*-body models (see Appendix A, Section A3). Although we found *stable* configurations in terms of the quadratic ephemeris, the semimajor axis of the outer companion is unconstrained (between 4 and at least 20 au). These stable fits exhibit varying sign of β (it means that the binary period might decrease or increase). Moreover, stable solutions with relatively small β may be found in very narrow stability zones in the (a_c, e_c) plane, see Appendix A and Fig. A6. These areas are associated with low-order MMRs, like 3c:2b MMR. It is very uncertain though, how massive companions of HU Aqr could be locked in such tiny stability areas. Hence, some larger values of a_c, providing extended zones of stable motions, seem more likely (see panels of stable fits labelled by IV, V and VI of Fig. A6). However, there is also a correlation between the magnitude of β and the semi-major axis of the outer planet. For relatively distant planet c, $|\beta|$ may be $\sim 2 \times 10^{-12}$ d cycle^{-2}, which is difficult to explain by magnetic braking or mass loss. However, this may indicate a presence of a third companion in an unconstrained orbit.

We conclude that these results seem to favour the one-planet hypothesis as the simplest model explaining the (O–C) variability, particularly in the light of very small rms of the homogeneous OPTIMA set and apparently perfect quasi-sinusoidal fit illustrated in Fig. 11.

6 RED NOISE AND/OR SYSTEMATIC ERRORS?

Analysis of the LTT observations has much in common with pulsar timing, planetary transits and precision radial velocity observations, which are modelled with least squares under the assumption that the measurement errors are uncorrelated (white noise). However, as is known particularly by pulsar observers, the assumption that white noise is the only source of error is unjustified when aiming at estimating the underlying model parameters and their uncertainties (Coles et al. 2011). In the past, this effect had been responsible for false detections of planets around pulsars (Bailes, Lyne & Shemar 1991). Similarly, correlated (red) noise or systematic errors have been found in the planetary transit data (Pont et al. 2006) and very recently, in the radial velocity measurements (Baluev 2011). The same type of non-Gaussian, low-frequency correlation of residuals to the orbital period of the binary may be present in the LTT data collected over long time intervals.

The danger of such systematic effects in the LTT-analysed binaries is reinforced due to their activity and complex astrophysical phenomena responsible for the observed emission. One of the already well recognized mechanisms able to produce cyclic variation of the orbital period of the binary has been proposed by Applegate (1992). As shown by this author, a magnetic star (here, the secondary) changes its internal structure due to magnetic cycles. The latter implies a variable zonal harmonic coefficient J_2 and subsequently, a variable gravitational tidal field for the orbital companion which results in a varying orbital period (Hilditch 2001). The Applegate mechanism as a possible origin of large (O–C) variations in the HU Aqr data was studied in detail by Vogel (2008), as well as by Schwarz et al. (2009). They discarded this possibility since the HU Aqr stellar set-up does not provide enough energy to drive changes of the orbital period. Similar results were obtained for the NN Ser system, that likewise has a low-mass, low-luminosity secondary star (Brinkworth et al. 2006) with a conclusion that it is incapable of driving significant period changes in terms of the Applegate model.

Another mechanism explaining observed long-term periodicities could be a slow precession of the rapidly spinning magnetic WD star, which has been proposed as a source of long periods detected in a few CVs, for instance FS Aur (Chavez et al. 2012) and V455 And (Tovmassian, Zharikov & Neustroev 2007). However, HU Aqr is unlikely to host such a WD, as this AM Her-like system is known to be synchronously locked. As a first, yet preliminary attempt, we tried to determine the characteristic that can be used to quantify the shapes of the HU Aqr light curves and might help to detect their variability and hence astrophysical sources of the LTT residuals. This approach mimics the bisector velocity span (BVS) technique used to detect distortion of spectral lines due to stellar spots and chromospheric activity. It is well known that stellar spots may produce apparent radial velocity changes up to 200 m s^{-1} (Berdyugina 2005). As a similar characteristic to the BVS, we choose the slope of the linear function fitted to the egress phase of the light curve, usually spanning no more than a few seconds interval. We analysed 59 available light curves in the precision OPTIMA set. The results are shown in Fig. 12. In seven cases, we decided the data were not precise enough to derive the slope reliably (as indicated by green filled squares) because of, for instance, bad weather or strong wind that could introduce telescope guidance errors. In a few other cases

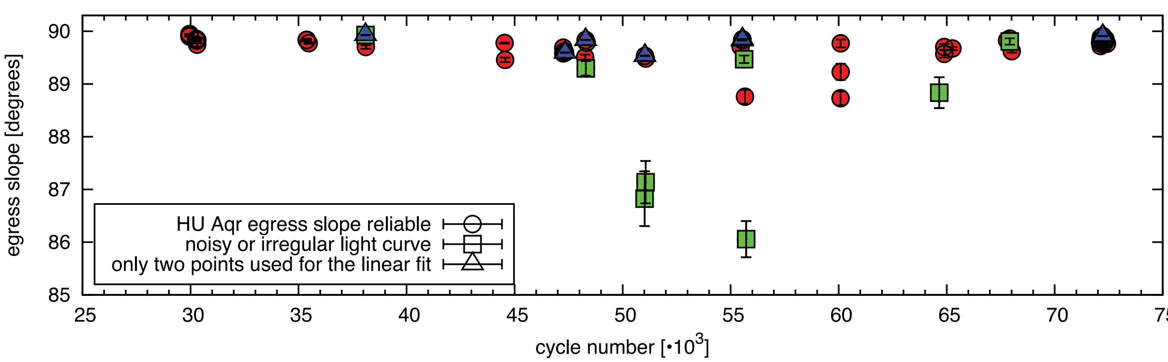

Figure 12. Linear slopes of 59 HU Aqr egresses derived on the basis of OPTIMA light curves by fitting a linear function only to the egress phase, usually spanning not more than a few seconds. In seven cases, the light curves were not precise enough (as indicated by green filled squares) because of a bad weather. In other seven cases, only two points were taken for the fit, therefore no error estimation was possible (blue triangles). See the text for more details.

(seven again, marked with blue triangles), only two points were taken for the fit, and therefore no error estimation was possible. Nevertheless, the obtained slopes are uniform and span less than 2° range close to 90°. That furthermore indicates a similarly rapid egress phase. The results of this test are encouraging, and support the planetary hypothesis.

However, the slopes should be best re-computed for all available light curves that were used to determine the egress times. The problem of the non-homogeneity of the collected light curves still exists. Because of varying eclipse profiles (e.g. during different accretion states), the determination of mid-egress dates is often very difficult. For instance, it could be prone to rather subjective choices of the photometric data range to fit the parameters of the sigmoid function, equation (12). That may introduce significant systematic errors, particularly if the reduction is performed by different researchers. This issue may be likely resolved by a re-analysis of the entire set of all available light curves, under similar conditions paying particular attention to their origin – the spectral window, an instrument, and even technical and observational circumstances.

Another direction still open is a study of the binary interactions, to eventually eliminate or discover astrophysical causes of the LTT variability. The problem is in fact universal and affects other techniques of extrasolar planets detection, such as pulsar timing and radial velocity monitoring of active or evolved stars, as well. It is yet possible that the observed (O–C) signal has both the planetary and unmodelled astrophysical component (Potter et al. 2011), making its unique resolution even harder.

To the best of our knowledge, possible effects of the red noise regarding the LTT observations have not been studied in detail. That problem certainly deserves a deep and careful investigation.

7 CONCLUSIONS

Using a new formulation of the LTT model of the (O–C) to the available data of the HU Aqr system, we found that the two-planet hypothesis by Qian et al. (2011) is not likely. Our results reinforce recent negative tests of dynamical stability of that system in the literature. The self-consistent LTT model presented in this work exhibits degenerate solutions, such as (apparently) Trojan objects of $\sim 10^4$ Jupiter masses, or a companion in a collisional/open parabolic or hyperbolic orbit. Ironically, two such solutions to the literature SSQ data are the best-fit models found in extensive, quasi-global searches adopting a hybrid optimization.

Moreover, on the basis of a much extended, precision data set, collected by the OPTIMA network, that increased the number of data points analysed in previous works by $\sim$50 per cent, we have shown that the observed (O–C) variations may be consistently explained by the presence of only one circumbinary planet of the minimal mass of $\sim$7 Jupiter masses, in an orbit with a small eccentricity of $\sim$0.1 and an orbital period of $\sim$10 yr, similar to Jupiter in the Solar system. Our results support the original one-planet hypothesis by Schwarz et al. (2009) rather than the two-planet model proposed by Qian et al. (2011). If confirmed, that planet would be the next circumbinary object detected from the ground, shortly after such companions have been announced around HW Vir (Lee et al. 2009), NN Ser (Beuermann et al. 2010), UZ For (Potter et al. 2011), SZ Her (Lee et al. 2012), FS Aur (Chavez et al. 2012) and DP Leo (Beuermann et al. 2011), followed by recent discoveries of Kepler-16b (Doyle 2011), Kepler-34b and Kepler-35b planets (Welsh et al. 2012). According to estimates by these authors, the observed rate of circumbinary planets around close binaries may be $\sim$1 per cent.

Furthermore, we found that the observations by Qian et al. (2011) are not confirmed by the OPTIMA measurements due to systematic relative shift of $\sim$3–10 s. The nature of this discrepancy is yet unknown. If the shift is caused by an error, all two-planet models presented in the literature that make use of their data are affected.

Besides the disagreement between our conclusions and the previous works, our results suggest that the kinematic modelling of two-planet configurations is not fully justified on the grounds of the dynamics because the best-fit models may imply large masses (up to stellar range), large eccentricities and similar orbital periods indicating a possibility of strong MMRs. Moreover, the (O–C) variability that suggests two-planet solutions most likely appears due to mixing observations done in different spectral windows. That feature of the data set – as we have shown here – introduces systematic effects that may alter the best-fit solutions significantly. This conclusion is supported by extensive numerical simulations of the two-planet systems dynamics by Horner et al. (2011), Wittenmyer et al. (2012) and Hinse et al. (2012). Considered within statistical error ranges, the initial conditions lead to catastrophically disruptive configurations, unconstrained elements of the outermost body, and/or period damping factor β.

In this work, we found best-fit stable two-planet models within the quadratic ephemeris N-body model to *all available data*, but the semimajor axis of the outer planet cannot be yet constrained. Stable configurations are located within low-order MMRs spanning tiny stable zones in the phase space, or are characterized by a large magnitude period decrease. In the first case, it is difficult to explain how a few Jupiter mass companions could be trapped in such particular, isolated resonances. In the second case, a large $|\beta|$ requires an efficient, internal mechanism of the binary period change, or indicates the presence of one more companion. Our findings might be a breakthrough after a few cited works reporting basically only unstable two-planet models of the HU Aqr system, but these discrepancies add even more ambiguity to the two-planet hypothesis.

However, the results of our experiments show that the one-planet solution is relatively well constrained by available *optical observations* selected as a homogeneous data set. Because the early optical data (the white light and V-band measurements) are coherent with an impressive, very clear quasi-sinusoidal signal exhibited by superior-precision OPTIMA measurements, as well as with the recent MONET/N, PIRATE and WFC data, a single-companion hypothesis seems well justified. A confirmation of the planetary origin of the LTT signal still requires long-term monitoring of the system. Because of its very long orbital period, it will take many years to confirm or reject the signal coherence. Such new data would be also very useful to constrain the orbital period by the recent OPTIMA observations alone.

ACKNOWLEDGMENTS

We thank the anonymous referee for a review and comments that improved the manuscript. We would like to thank Maciej Konacki (CAMK Toruń) for a discussion and a suggestion of the egress slopes test, as well as Anna Zajczyk (CAMK, Toruń), Andrzej Szary (UZG, Zielona Góra), Alex Stefanescu, Martin Mühlegger, Helmut Steinle, Natalia Primak, Fritz Schrey and Christian Straubmeier (all MPE) for their help with observations. KG is supported by the Polish Ministry of Science and Higher Education Grant No. N/N203/402739 and POWIEW project of the European Regional Development Fund in Innovative Economy Programme POIG.02.03.00-00-018/08. IN acknowledges support from the EU FP6 Transfer of Knowledge Project 'Astrophysics of Neutron Stars' (MKTD-CT-2006-042722). AS would like to thank Bronek Rudak for his support and discussions. She also acknowledges support from the Foundation for Polish Science grant FNP HOM/2009/11B, as well as from the Marie Curie European Reintegration Grant within the 7th European Community Framework Programme (PERG05-GA-2009-249168). GK acknowledges support from the EU FP6 Transfer of Knowledge Project ASTROCENTER (MTKD-CT-2006-039965) and the kind hospitality of the Skinakas team at UoC. BG thanks the Wide FastCam team for help in performing the observations. Research by TCH is carried out under the KRCF Young Researcher Fellowship Program at the Korea Astronomy and Space Science Institute. NH acknowledges support from the NASA Astrobiology Institute under Cooperative Agreement NNA09DA77A at the Institute for Astronomy, University of Hawaii, and from NASA/EXOB program under grant NNX09AN05G. We thank the Skinakas Observatory for their support and allocation of telescope time. Skinakas Observatory is a collaborative project of the University of Crete, the Foundation for Research and Technology – Hellas, and the Max-Planck-Institute for Extraterrestrial Physics. This paper is based on observations made with the TCS telescope operated on the island of Tenerife by the Instituto de Astrofisica de Canarias in the Spanish Teide Observatory. This work is based in part on data obtained with the MONET, funded by the Alfried Krupp von Bohlen und Halbach Foundation, Essen, and operated by the Georg-August-Universität Göttingen, the McDonald Observatory of the University of Texas at Austin and the South African Astronomical Observatory.

REFERENCES

Applegate J. H., 1992, ApJ, 385, 621
Bailes M., Lyne A. G., Shemar S. L., 1991, Nat, 352, 311
Baluev R. V., 2011, Celest. Mech. Dynamical Astron., 111, 235
Beard S. M., Vick A. J. A., Atkinson D., Dhillon V. S., Marsh T., McLay S., Stevenson M., Tierney C., 2002, in Lewis H., ed., Proc. SPIE Vol. 4848, Advanced Telescope and Instrumentation Control Software II. SPIE, Bellingham, p. 218
Berdyugina S. V., 2005, Living Rev. Sol. Phys., 2, 8
Beuermann K. et al., 2010, A&A, 521, L60
Beuermann K. et al., 2011, A&A, 526, A53
Brinkworth C. S., Marsh T. R., Dhillon V. S., Knigge C., 2006, MNRAS, 365, 287
Charbonneau P., 1995, A&AS, 101, 309
Chavez C. E., Tovmassian G., Aguilar L. A., Zharikov S., Henden A. A., 2012, A&A, 538, A122
Cincotta P. M., Giordano C. M., Simó C., 2003, Physica D, 182, 151
Coles W., Hobbs G., Champion D. J., Manchester R. N., Verbiest J. P. W., 2011, MNRAS, 418, 561
Dhillon V. S. et al., 2007, MNRAS, 378, 825
Doyle L. R., et al., 2011, Sci, 333, 1602
Eastman J., Siverd R., Gaudi B. S., 2010, PASP, 122, 935
Goździewski K., Konacki M., 2004, ApJ, 610, 1093
Goździewski K., Maciejewski A. J., 2001, ApJ, 563, L81
Goździewski K., Konacki M., Maciejewski A. J., 2003, ApJ, 594, 1019
Goździewski K., Migaszewski C., Musieliński A., 2008, in Sun Y.-S., Ferraz-Mello S., Zhou J.-L., eds, Proc. IAU Symp. 249, Stability Constraints in Modeling of Multi-Planet Extrasolar Systems. Cambridge Univ. Press, Cambridge, p. 447
Hairer E., Nærsett S. P., Wanner G., 2009, Solving Ordinary Differential Equations I: Nonstiff Problems. Springer-Verlag, Berlin
Hellier C., 2001, Cataclysmic Variable Stars – How and Why they Vary. Springer-Verlag, Berlin
Hilditch R. W., 2001, An Introduction to Close Binary Stars. Cambridge Univ. Press, Cambridge, p. 392
Hinse T. C., Lee J. W., Goździewski K., Haghighipour N., Lee C.-U., Scullion E. M., 2012, MNRAS, 420, 3609
Holmes S. et al., 2011, PASP, 123, 1177
Horner J., Marshall J. P., Wittenmyer R. A., Tinney C. G., 2011, MNRAS, 416, L11
Irwin J. B., 1952, ApJ, 116, 211
Kanbach G., Kellner S., Schrey F. Z., Steinle H., Straubmeier C., Spruit H. C., 2003, in Iye M., Moorwood A. F. M., eds, Proc. SPIE Vol. 4841, Instrument Design and Performance for Optical/Infrared Ground-based Telescopes. SPIE, Bellingham, p. 82
Kanbach G., Stefanescu A., Duscha S., Mühlegger M., Schrey F., Stele H., Slowikowska A., Spruit H., 2008, in Phelan D., Ryan O., Shearer A., eds, Astrophys. Space Sci. Lib. Vol. 351, High Time Resolution Astrophysics. Springer-Verlag, Berlin, p. 153
Laughlin G., Chambers J. E., 2001, ApJ, 551, L109
Lee M. H., Peale S. J., 2003, ApJ, 592, 1201
Lee J. W., Kim S.-L., Kim C.-H., Koch R. H., Lee C.-U., Kim H. I., Park J.-H., 2009, AJ, 137, 3181
Lee J. W., Lee C.-U., Kim S.-L., Kim H. I., Park J.-H., 2012, AJ, 143, 34
Malhotra R., 1993, in Phillips J. A., Thorsett S. E., Kulkarni S. R., eds, ASP Conf. Ser. Vol. 36, Planets Around Pulsars. Astron. Soc. Pac., San Francisco, p. 89
Morbidelli A., 2002, Modern Celestial Mechanics: Aspects of Solar System Dynamics. Taylor & Francis, London
Nasiroglu I., Słowikowska A., Kanbach G., Schwarz R., Schwope A. D., 2010, in Proc. Sci., High Time Resolution Astrophysics (HTRA) IV – The Era of Extremely Large Telescopes. http://pos.sissa.it/cgi-bin/reader/conf.cgi?confid=108
Pont F., Zucker S., Queloz D., 2006, MNRAS, 373, 231
Potter S. B. et al., 2011, MNRAS, 416, 2202
Press W. H., 2002, Numerical Recipes in C++: The Art of Scientific Computing. Cambridge Univ. Press, Cambridge
Qian S.-B. et al., 2011, MNRAS, 414, L16
Schwarz R., Schwope A. D., Vogel J., Dhillon V. S., Marsh T. R., Copperwheat C., Littlefair S. P., Kanbach G., 2009, A&A, 496, 833
Schwope A. D., Schwarz R., Sirk M., Howell S. B., 2001, A&A, 375, 419
Schwope A. et al., 2004, in Vrielmann S., Cropper M., eds, IAU Colloq. 190, ASP Conf. Ser. Vol. 315, Magnetic Cataclysmic Variables. Astron. Soc. Pac., San Francisco, p. 92
Schwope A. D., Horne K., Steeghs D., Still M., 2011, A&A, 531, A34
Słonina M., Goździewski K., Migaszewski C., 2012, in Arenou F., Hestroffer D., eds, Orbital Couples: Pas de Deux in the Solar System and the Milky Way. preprint (arXiv:1202.6513v1)
Tovmassian G. H., Zharikov S. V., Neustroev V. V., 2007, ApJ, 655, 466
Vogel J., 2008, PhD thesis, Technischen Universität Berlin, Germany
Vogel J., Schwope A., Schwarz R., Kanbach G., Dhillon V. S., Marsh T. R., 2008, in Phelan D., Ryan O., Shearer A., eds, AIP Conf. Ser. Vol. 984, High Time Resolution Astrophysics: The Universe at Sub-Second Timescales. Am. Inst. Phys., New York, p. 264
Warner B., 1995, Cambridge Astrophys. Ser. Vol. 28, Cataclysmic Variable Stars. Cambridge Univ. Press, Cambridge
Welsh W. F. et al., 2012, Nat, 481, 475
Wittenmyer R. A., Horner J., Marshall J. P., Butters O. W., Tinney C. G., 2012, MNRAS, 419, 3258

APPENDIX A: ALTERNATE MODELS TO ALL DATA

In this section, we describe supplementary results illustrating a few alternative models to the one-planet solution of the (O–C) of the HU Aqr binary that was analysed in the main part of the paper. Basically, all 171 data points are modelled, although in some cases, we removed outlying data from Qian et al. (2011) because they clearly introduce a systematic error. We considered one-planet model with a heuristic, sine-damping term (Section A1), two-planet kinematic models (Section A2) and the full, two-planet, self-consistent Newtonian model (Section A3). The aim of this appendix is to

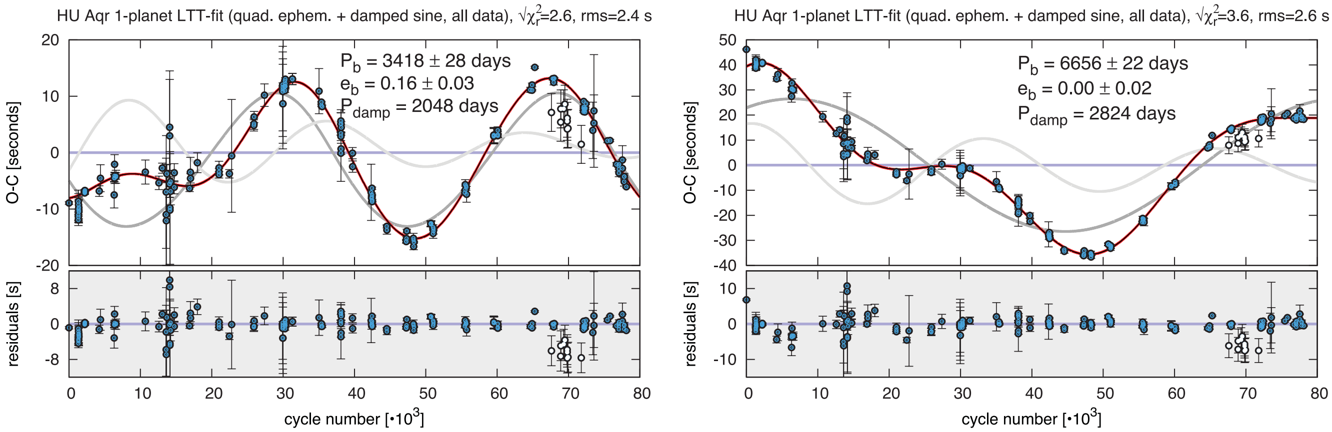

Figure A1. Examples of synthetic curves of the one-planet LTT quadratic ephemeris models with a sine damping term to all 171 data points gathered in this work, including 10 measurements in Qian et al. (2011), marked with white filled circles. The shaded curves represent the planetary and the damped sine signal, respectively.

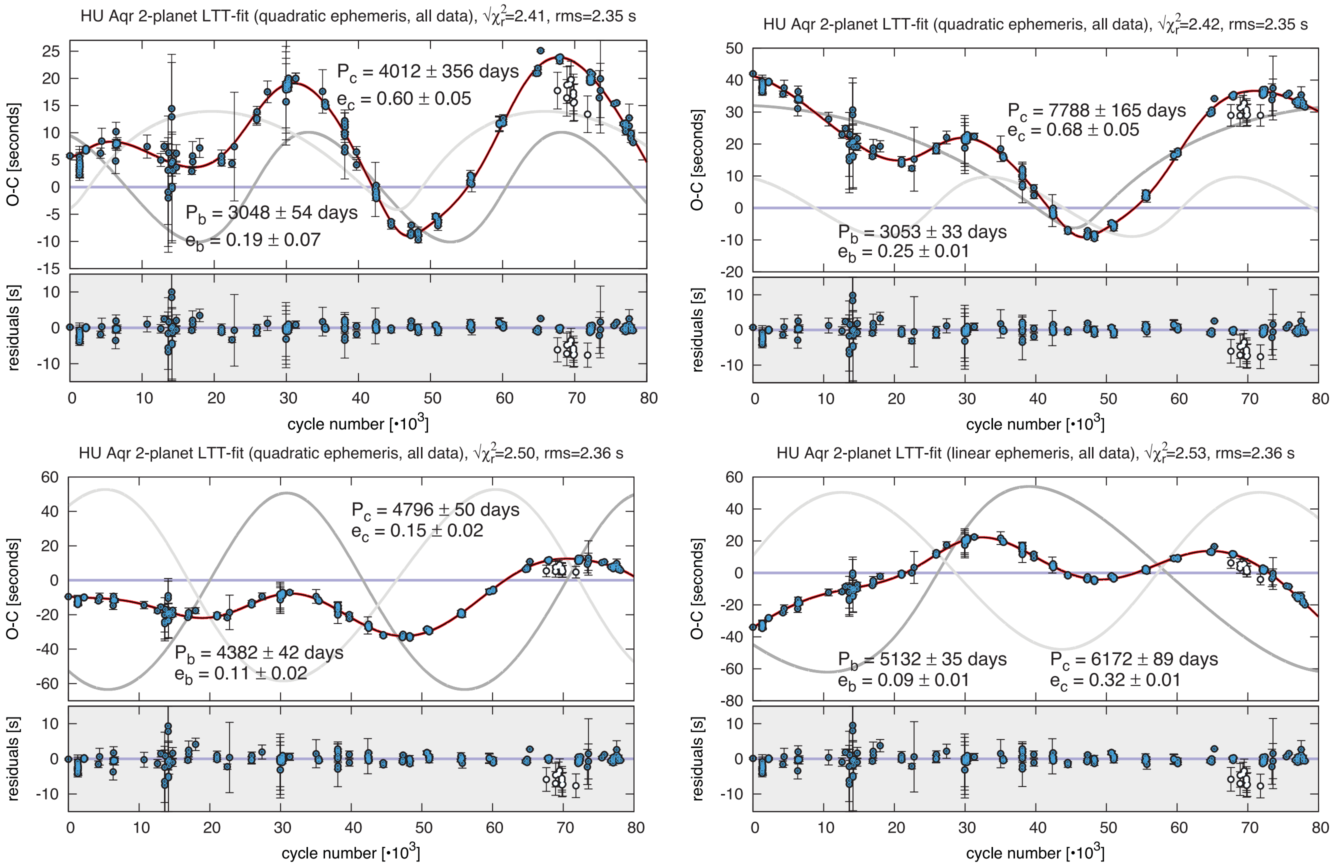

Figure A2. Examples of synthetic curves of the two-planet LTT quadratic and linear (bottom right-hand panel) ephemeris models to all 171 data points analysed in this work, including 10 data points in Qian et al. (2011) which are marked with white filled circles. The shaded curves represent single planetary signal terms, respectively.

demonstrate that two-planet models lead to non-unique or unconstrained solutions. Hence, these results reinforce the hypothesis of a single, quasi-sinusoidal signal of possibly planetary origin.

A1 Quadratic ephemeris one-planet model with damping term

To describe the suggested damping signal visible in Fig. 8 (top right-hand panel), we modified the quadratic ephemeris model by adding a heuristic term having the following form:

$$\tau_{\rm damp}(t) = \tau_0 + A \exp(-t/T_{\rm damp}) \sin(n_{\rm damp}\, t + \phi_0), \qquad \text{(A1)}$$

where τ_0 is an offset, A is the semi-amplitude of the signal, $T_{\rm damp}$ is the damping time-scale, $n_{\rm damp} = 2\pi/P_{\rm damp}$ is the frequency and ϕ_0 is the initial phase at epoch $l = 0$. Two examples of best-fit solutions to all available data (171 measurements) are shown in Fig. A1. Let us note that the planetary orbital period in the

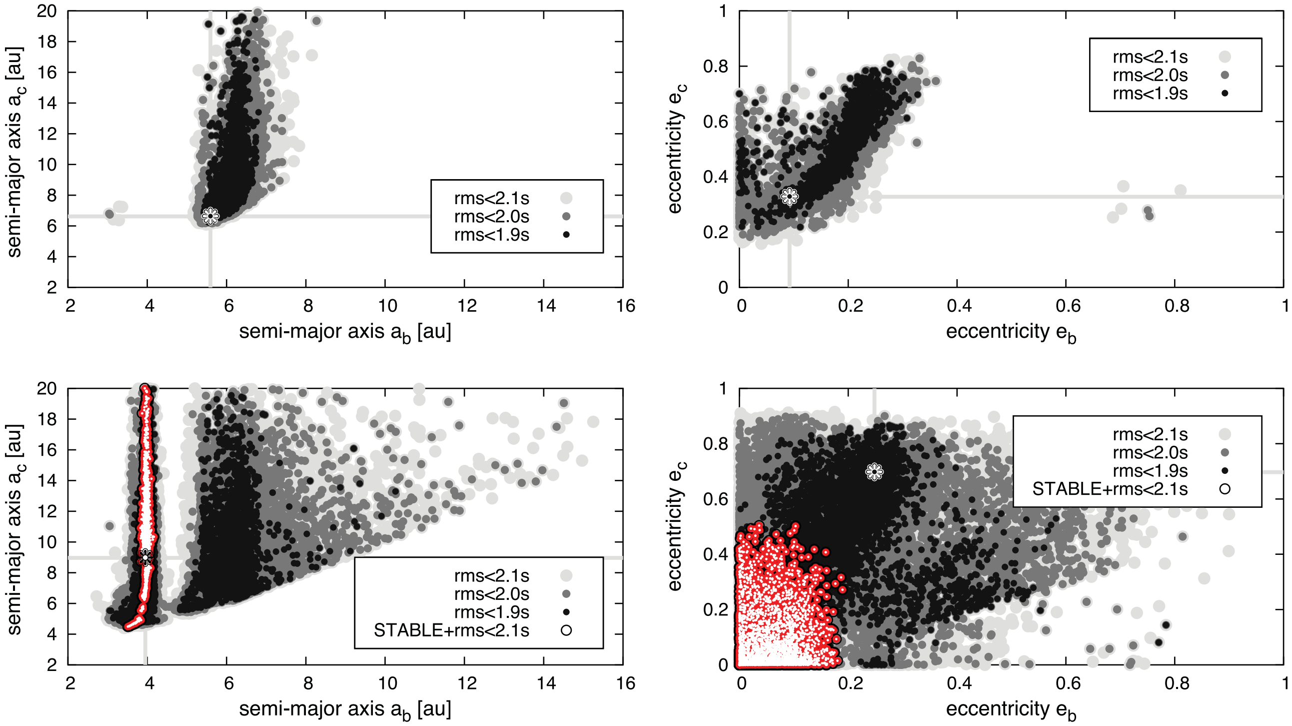

Figure A3. Statistics of two-planet N-body models gathered with the hybrid algorithm, projected on to planes of selected parameters. Top row illustrates the results for the linear ephemeris, bottom row shows the fits for the quadratic ephemeris model. The rms quality of these solutions is coded as filled circles: the better fit – the darker colour. Orbital parameters of the best-fit solutions are marked with shaded, intersecting lines and a flower symbol. Solutions Lagrange stable over 10^6 revolutions of the outermost planet are marked with red–white circles.

configuration in the right-hand panel of this figure is twice the period in the one-planet model studied earlier. The (O–C) of a solution shown in the left-hand panel cannot be distinguished from two-planet models (see the text below).

The physical nature of the damped signal is uncertain. Allowing for some speculations, the damping might appear due to a long-term relaxation in the binary system which may, for instance, be due to the binary's magnetic cycles (Applegate mechanism). In such a case, the observed LTT signal would be resulted from two distinct phenomena. However, we recall here that Vogel (2008) and Schwarz et al. (2009) estimated that the Applegate mechanism cannot be responsible for orbital changes of HU Aqr.

A2 Kinematic two-planet models

We also tested two-planet models with the linear and quadratic ephemeris, (equations 10 and 11). Examples of the best-fit configurations with comparable $(\chi^2_\nu)^{1/2}$ and rms are shown in Fig. A2. Similar to the case of the SSQ data set, no unique solution may be found. For the parabolic ephemeris, we found many similar-quality best-fit solutions. These fits are characterized by the orbital periods ratio close to 1c:1b MMR with inferred planetary masses of $\sim 20\,M_{\rm Jup}$ (bottom left-hand panel in Fig. A2), close to 4c:3b MMR with inferred masses of ~ 5.5 and $\sim 4.0\,M_{\rm Jup}$ (top right-hand panel in Fig. A2). A solution close to the 2c:1b MMR (top right-hand panel in Fig. A2), as well as configurations with extreme eccentricity $e_c \sim 0.95$, *positive* damping factor $\beta \sim 10^{-12}$ cycles d^{-2}, and unconstrained $P_c \sim 250\,000$ d (not shown here) were also found. In all these cases, the rms remains at the level of 2.4 s. Some of these solutions are qualitatively similar to the two-planet fits found for the SSQ data set. These results imply that the significantly extended data set still does not constrain two-planet models.

For the linear ephemeris model, we found one best-fit solution that frequently appeared in different runs of the hybrid code. It is shown in the bottom right-hand panel of Fig. A2. This solution is characterized by an orbital periods ratio close to 6:5. Taken literally, this fit corresponds to Trojan brown dwarfs. However, the kinematic model is inadequate for such a configuration of massive objects.

A3 Newtonian, self-consistent N-body two-planet models

In the light of the discussion presented above, we performed a preliminary modelling of all available data with the help of the hybrid algorithm driven by the self-consistent N-body model. Moreover, we tested Lagrange stability of the best-fit models following their orbital evolution over at least 10^6 orbital periods of the outermost planet. Configurations which survived during such time without a collision or remaining on closed orbits were regarded stable. In this experiment we use 161 data points, excluding data in Qian et al. (2011), due to the discrepancy with OPTIMA measurements.

To illustrate the results of the hybrid optimization, we projected the found solutions on to particular planes of the Keplerian astrocentric, osculating elements of the planets (Fig. A3) at the epoch of the first observation. The general finding is that the N-body formulation helps to improve the rms that decreased from ~ 2.4 to ~ 1.9 s as compared to kinematic models.

Top row of Fig. A3 illustrates the results for the linear ephemeris. Clearly, the data do not constrain the semimajor axes and eccentricities of the companions. The eccentricities tend to be large, up to 0.8. Moreover, the best-fit configuration exhibit similar values of semimajor axes (~ 5.6 and ~ 6.3 au) and large masses in the brown dwarfs range of ~ 20 Jupiter masses. We did not find any

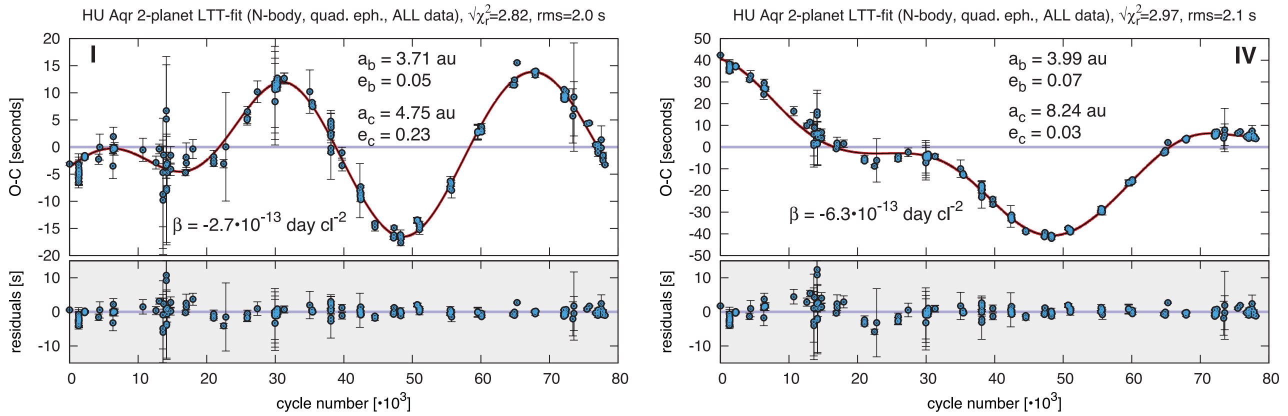

Figure A4. Examples of synthetic LTT curves and (O–C) residuals for *stable* two-planet quadratic ephemeris Newtonian (N-body) models to 161 data points analysed in this work, without 10 data points in Qian et al. (2011). These models are selected from a sample illustrated in Fig. A3. Dynamical maps of these solutions show Fig. A5 (they are labelled with the Roman numerals, as I and IV, respectively).

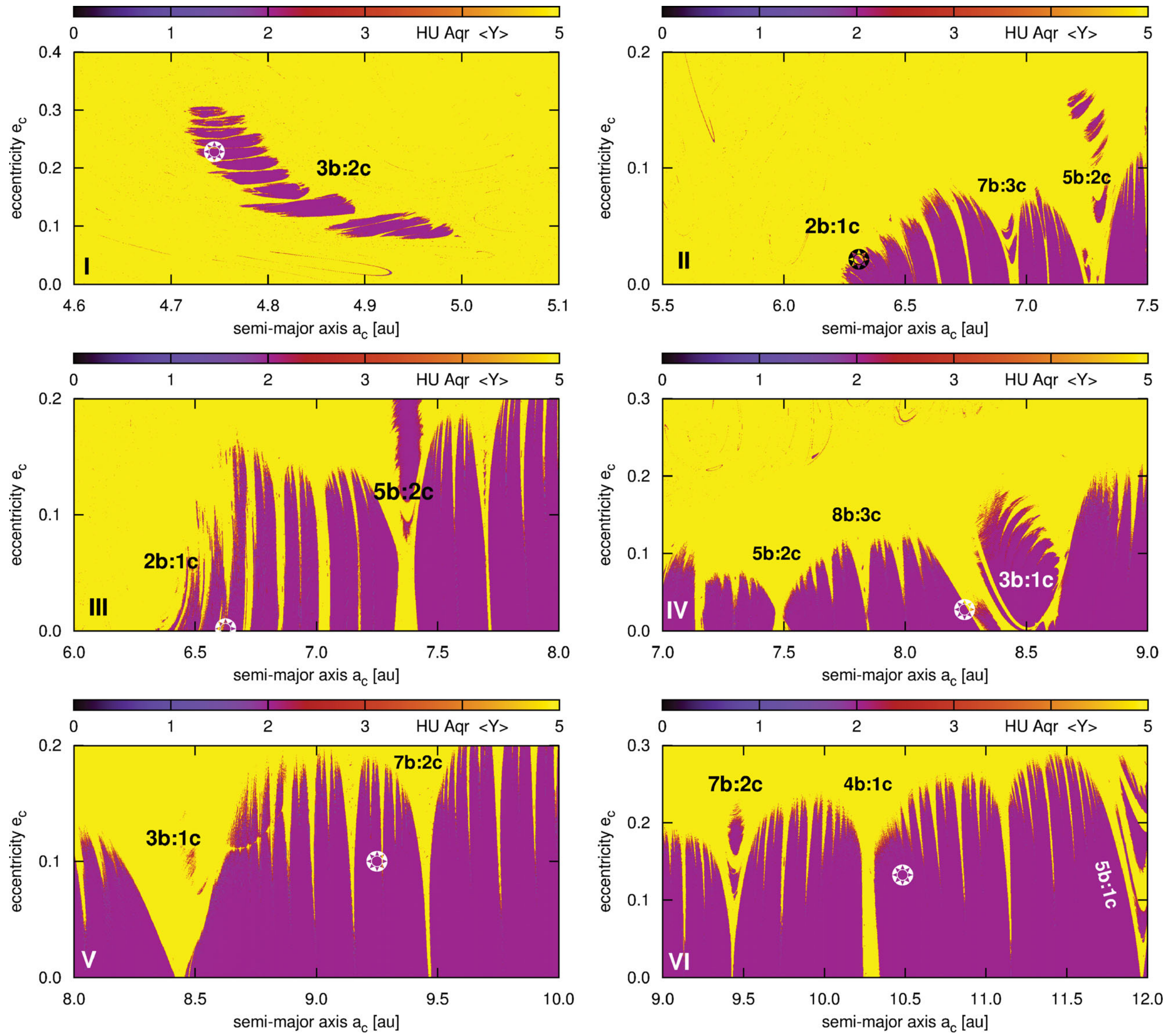

Figure A5. MEGNO dynamical maps in the (a_c, e_c) plane for a few representative N-body *stable* solutions illustrated in the bottom panels of Fig. A4. Yellow colour encodes strongly unstable (chaotic) configurations, and purple colour (MEGNO $\langle Y \rangle \sim 2$) is for stable, quasi-periodic solutions. Parameters of the nominal, tested fits are marked with the star symbol. The most prominent, low-order MMRs are labelled. The original resolution of these dynamical maps is 1440×900 data points integrated for 10^4 outermost orbital period each. The total mass of the binary is 0.98 $M_\odot$ (Schwope et al. 2011).

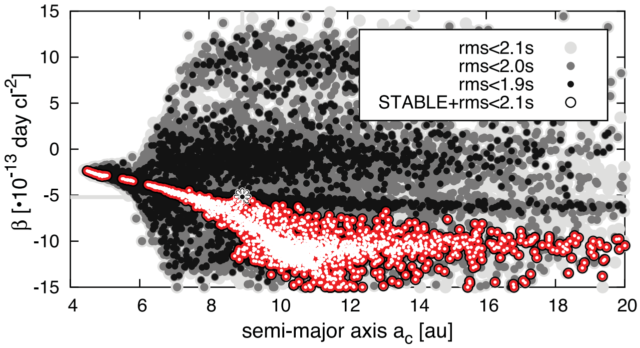

Figure A6. Statistics of two-planet *N*-body quadratic ephemeris models gathered with the hybrid algorithm, projected on to the (a_c, β) plane, for the quadratic ephemeris. Meaning of symbols is the same as in Fig. A3.

stable configurations within this model. It is consistent with the results for the SSQ data set (Hinse et al. 2012).

Interesting results are obtained for the quadratic ephemeris model (see bottom row in Fig. A2) although this model also does not constrain orbital parameters, due to even larger spread of the semimajor axes and eccentricities than in the linear ephemeris model. Two minima of $(\chi_\nu^2)^{1/2}$ are found, around $a_b \sim 4$ and $\sim$6 au, respectively. The best-fit configurations have $(\chi_\nu^2)^{1/2} \sim 2.6$ and an rms $\sim$1.9 s that is $\sim$20 per cent better than for those best kinematic models. In the neighbourhood of the first $(\chi_\nu^2)^{1/2}$ minimum ($a_b \sim 4$ au), we found a few thousands of Lagrange stable models characterized by $(\chi_\nu^2)^{1/2} < 3$ and an rms <2.1 (still better than for those best two-planet kinematic models). These fits have well bounded $a_b \sim 4$ au and small eccentricities up to 0.4. However, the osculating semimajor axis of the outer body is unconstrained and covers many low-order MMRs, between 3c:2b MMR and 5c:1b MMR. Fig. A4 shows synthetic curves of two example solutions corresponding to the 3c:2b MMR (left-hand panel) and for a model close to 3c:1b MMR (right-hand panel). To identify these resonances, in the neighbourhoods of a few selected best-fit models, we derived high-resolution dynamical maps (1440 × 900 data points) shown in Fig. A5. These maps are computed in terms of the fast indicator Mean Exponential Growth factor of Nearby Orbits (MEGNO; Cincotta, Giordano & Simó 2003), with the help of our recently developed CPU cluster software MECHANIC[3] (Słonina, Goździewski & Migaszewski 2012). MEGNO measures the maximal Lyapunov exponent, which makes it possible to distinguish between chaotic and regular solutions. Each point at these maps has been integrated over $\sim 10^4$ orbital periods of the outermost companion. The dynamical maps confirm that the Lagrange stable models examined over a limited time-span are equivalent to quasi-periodic, stable solutions.

A solution illustrated in the left-hand panel of Fig. A4 is the best-fit *stable* model found in the hybrid search with $(\chi_\nu^2)^{1/2} \sim 2.82$ and an rms $\sim$2 s. It is located in a very narrow, isolated stability island of the 3c:2b MMR and characterized by relatively large $\beta \sim -2.7 \times 10^{-13}$ d cycle^{-2}, similar to the kinematic model. The right-hand panel of Fig. A4 shows a configuration close to the 3c:1b MMR, which has even larger $\beta \sim -6 \times 10^{-13}$ d cycle^{-2}.

Fig. A6 shows a statistics of the best-fit solutions in the (a_c, β) plane. It reveals that β is not constrained, regarding even its sign. Stable models exhibit a strong correlation between both these parameters. A larger value of the semimajor axis of the outer planet is related to a larger magnitude of β. Because of this correlation, an interpretation of stable configurations is complex. For relatively small magnitude of β, stable configurations are characterized by low-order MMRs and may be found in tiny areas of stable motions (see Fig. A5). For more separated planets, when stability zones are much more extended, $|\beta|$ increases. Already $|\beta| \sim 2 \times 10^{-13}$ d cycle^{-2} is difficult to explain by physical phenomena in the binary, as we discussed in Section 5. Such large values of $|\beta|$ may indicate a third, long-period companion object in a very distant orbit. However, because already the two-planet model is not constrained by the data, also a three-planet configuration cannot be fixed without ambiguity. We did an attempt to search for such Newtonian three-planet models within the linear ephemeris, but we did not find any improved, nor stable solutions of this type.

[3] http://git.astri.umk.pl/projects/mechanic

This paper has been typeset from a TEX/LATEX file prepared by the author.